

1 Extending the tephra and palaeoenvironmental record of the Central 2 Mediterranean back to 430 ka: A new core from Fucino Basin, central Italy

3
4
5 Biagio Giaccio^{a,b*}, Niklas Leicher^c, Giorgio Mannella^d, Lorenzo Monaco^e, Eleonora Regattieri^{d,f}, Bernd
6 Wagner^c, Giovanni Zanchetta^{d,a}, Mario Gaeta^e, Fabrizio Marra^b, Sébastien Nomade^g, Danilo M. Palladino^e,
7 Alison Pereira^{g,h,i,j}, Stephanie Scheidt^c, Gianluca Sottili^e, Thomas Wonik^k, Sabine Wulf^f, Christian Zeeden^k,
8 Daniel Ariztegui^m, Gian Paolo Cavinato^a, Jonathan R. Deanⁿ, Fabio Florindo^b, Melanie J. Leng^{o,p}, Patrizia
9 Macri^b, Elizabeth Niespolo^{q,r}, Paul R. Renne^{q,r}, Christian Rolf^k, Laura Sadori^s, Camille Thomas^m,
10 Polychronis C. Tzedakis^t

11
12
13 ^a Istituto di Geologia Ambientale e Geoingegneria, CNR, Rome, Italy

14 ^b Istituto Nazionale di Geofisica e Vulcanologia, Sezione Roma I, Rome, Italy

15 ^c Institute of Geology and Mineralogy, University of Cologne, Cologne, Germany

16 ^d Dipartimento di Scienze della Terra, University of Pisa, Pisa, Italy

17 ^e Dipartimento di Scienze della Terra, Sapienza-Università di Roma, Rome, Italy

18 ^f Istituto di Geoscienze e Georisorse, CNR, Pisa, Italy

19 ^g Laboratoire des Sciences du Climat et de l'Environnement (CEA-CNRS-UVSQ), Université Paris-Saclay, Gif sur Yvette, France

20 ^h École Française de Rome, Rome, Italy

21 ⁱ UMR 7194 HNHP, Département Homme et Environnement, Muséum national d'Histoire naturelle, Paris, France

22 ^j Sezione di Scienze Preistoriche e Antropologiche, Dipartimento di Studi Umanistici, Università degli Studi di Ferrara, Ferrara, Italy

23 ^k Leibniz Institute for Applied Geophysics (LIAG), Hannover, Germany

24 ^l School of the Environment, Geography and Geosciences, University of Portsmouth, Portsmouth, UK

25 ^m Department of Earth Sciences, University of Geneva (UNIGE), Geneva, Switzerland

26 ⁿ Department of Geography, Geology and Environment University of Hull, Hull, UK

27 ^o Centre for Environmental Geochemistry, School of Geography, University of Nottingham, Nottingham, UK

28 ^p National Environmental Isotope Facility, British Geological Survey, Keyworth, Nottingham, UK

29 ^q Department of Earth and Planetary Science, University of California, Berkeley, USA

30 ^r Berkeley Geochronology Center, Berkeley, USA

31 ^s Dipartimento di Biologia Ambientale, University of Roma "La Sapienza", Rome, Italy

32 ^t Environmental Change Research Centre, Department of Geography, University College London (UCL), London, UK

33 34 Abstract

35 Here we present the first tephrostratigraphic, palaeomagnetic, and multiproxy data from a new ~98 m-deep
36 sediment core retrieved from the Fucino Basin, central Italy, spanning the last ~430 kyr. Palaeoenvironmental
37 proxy data (Ca-XRF, gamma ray and magnetic susceptibility) show a cyclical variability related to interglacial-
38 glacial cycles since the Marine Isotope Stage (MIS) 12-MIS 11 transition. More than 130 tephra layers are
39 visible to the naked eye, 11 of which were analysed (glass-WDS) and successfully correlated to known
40 eruptions and/or other equivalent tephra. In addition to tephra already recognised in the previously investigated
41 cores spanning the last 190 kyr, we identified for the first time tephra from the eruptions of: Tufo Giallo di
42 Sacrofano, Sabatini (288.0 ± 2.0 ka); Villa Senni, Colli Albani (367.5 ± 1.6 ka); Pozzolane Nere and its
43 precursor, Colli Albani (405.0 ± 2.0 ka, and 407.1 ± 4.2 ka, respectively); and Castel Broco, Vulcini (419-490
44 ka). The latter occurs at the bottom of the core and has been $^{40}\text{Ar}/^{39}\text{Ar}$ dated at 424.3 ± 3.2 ka, thus providing
45 a robust chronological constrain for both the eruption itself and the base of the investigated succession. Direct
46 $^{40}\text{Ar}/^{39}\text{Ar}$ dating and tephra geochemical fingerprinting provide a preliminary radioisotopic-based
47 chronological framework for the MIS 11-MIS 7 interval, which represent a foundation for the forthcoming
48 multiproxy studies and for investigating the remaining ~110 tephra layers that are recorded within this interval.
49 Such future developments will be contribute towards an improved MIS 11-MIS 7 Mediterranean
50 tephrostratigraphy, which is still poorly explored and exploited.

54 1. Introduction

55 High-precision chronologies and reliable correlations of sedimentary records are fundamental requirements
56 for reconstructing the Earth's history and evaluating the role of the processes underlying its evolution. This is
57 particularly true for palaeoenvironmental and palaeoclimatic studies dealing with Quaternary orbital and
58 millennial-scale variability. Our understanding of the spatial-temporal variability, magnitude, regional
59 expressions, and underlying mechanisms of the triggering, propagation, and sustaining of past climate change
60 is dependent on high-quality and high-resolution proxy series, provided that they are anchored to precise and
61 accurate time scales (e.g., Govin et al., 2015). The lack of robust chronologies also limits the use of data for
62 testing climate models, which are fundamental for understanding the climate system and forecasting future
63 change.

64 Alongside the growing need of more accurate, precise, and high-resolution chronologies in sedimentary
65 archives, the study of distal tephra has experienced an outstanding surge during the last decade (e.g., Lane et
66 al., 2017). Diagnostic geochemical features of tephra components (e.g., glass, minerals) allow the
67 unambiguous identification and tracking of tephra layers in different sedimentary settings, thus providing us
68 with a unique tool to establish stratigraphic correlations between sedimentary archives (tephrostratigraphy)
69 and to transfer radioisotopic ages of these layers (tephrochronology) over wide regions.

70 The relevance of tephra studies is clearly highlighted in large international projects and working groups, such
71 as RESET (REsponse of humans to abrupt Environmental Transitions; e.g., Lowe et al., 2015) and INTIMATE
72 (INTegration of Ice core, MARine and TERrestrial records of the Last Termination; e.g., Blockley et al., 2014),
73 which have drawn attention and prompted the development and application of tephrochronology. Furthermore,
74 tephrochronology has also been shown to be vital in several of the recent continental (ICDP) deep drilling
75 projects (e.g., PASADO, Wastegård et al., 2013; PALAEOVAN, Litt and Anselmetti, 2014; SCOPSCO,
76 Leicher et al., 2016). In spite of these efforts a satisfactory and reliable tephra framework for the Mediterranean
77 region is available only for the 200 kyr (Bourne et al., 2010; 2015; Giaccio et al., 2012b; 2017; Insinga et al.,
78 2014; Paterne et al., 2008; Petrosino et al., 2016; Smith et al., 2011; Sulpizio et al., 2010; Tamburrino et al.,
79 2012; Tomlinson et al., 2014; Wulf et al., 2004; 2012; Zanchetta et al., 2008; 2018). Extending the use of
80 tephrochronology for extra-regional to global scale chronological purposes beyond the current relatively short
81 temporal limits of the Upper Pleistocene has thus become an urgent need.

82 Reliable tephrostratigraphies can be best achieved in regions characterised by: (i) intense and frequent
83 Quaternary potassic-ultrapotassic explosive volcanism, that allow high-precision $^{40}\text{Ar}/^{39}\text{Ar}$ dating, and by (ii)
84 the presence of nearby, long and continuous sedimentary archives that in addition to the recording of tephra
85 provide detailed palaeoclimatic and palaeoenvironmental information. In the central Mediterranean region, the
86 Plio-Quaternary lacustrine successions hosted in the Central-Southern Apennine intermountain tectonic
87 depressions (e.g., Galadini et al., 2003) are among the few sedimentary archives that fulfil both these
88 requirements. These archives record in detail the environmental and climatic history (e.g., Karner et al., 1999;
89 Giaccio et al., 2015a; Mannella et al., 2019; Regattieri et al., 2015; 2016; 2017; 2019; Russo Ermolli et al.
90 2015) and contain frequently deposited tephra layers from adjacent ultrapotassic peri-Tyrrhenian, high-
91 explosive volcanic centres that can be $^{40}\text{Ar}/^{39}\text{Ar}$ dated (e.g., Karner et al., 1999; Giaccio et al., 2012a; 2013b;
92 2014; 2017; Amato et al., 2014; Petrosino et al., 2014b) (Fig. 1). Among these, the Fucino Basin, located in
93 the centre of the Central Apennines (Fig. 1), is a key archive as first studies of its uppermost lacustrine
94 succession (<190 ka) have demonstrated the potential for retrieving a long and continuous record of both past
95 volcanic activity and environmental changes (Di Roberto et al., 2018; Giaccio et al., 2015b; Giaccio et al.,
96 2017; Mannella et al., 2019).

97 In June 2017, a new scientific drilling campaign was conducted with the aim of extending the available Fucino
98 record back in time and of exploring its actual potential, in terms of sedimentary continuity and wealth of both
99 tephra and palaeoclimatic proxy data. Here we present the first results of ongoing studies on the new F4-F5
100 core (Fig. 1) and provide a preliminary chronological and palaeoenvironmental framework for the forthcoming
101 high-resolution, multiproxy investigations.

102
103
104
105
106
107
108
109
110
111
112
113
114
115
116
117
118
119
120
121
122
123
124
125
126
127
128
129
130
131
132
133
134
135
136
137
138
139
140
141
142
143
144
145
146
147
148
149

2. Geological, structural and stratigraphic setting of the Fucino Basin

The Fucino Basin (coordinates of the basin's midpoint: 42° 00' 00" N; 13° 30' 00" E) is located at ~650 m a.s.l and is surrounded by some of the highest peaks of the Central Apennine, which hosted mountain glaciers during glacial periods (e.g., Giraudi and Giaccio, 2015). Until recently, the Fucino Basin hosted Lake Fucinus, which covered a surface area of 150 km² prior to its partial drainage during the 1st-2nd century AD, which was completed at the end of the 19th century.

The basin is bounded to the ENE by normal faults of the Fucino Fault System (FFS; Galadini and Galli, 2000). The FFS is the main, currently active, tectonic structure responsible for the Plio-Pleistocene opening and evolution of the Fucino Basin (Cavinato et al., 2002), as well as for generating high magnitude (Mw 7.0) historical earthquakes (Galli et al., 2016). Longitudinal and transverse seismic lines crossing the basin with respect to the NW-SE strike of the FFS, depict a semi-graben geometry with increasing thickness of the sedimentary infill from the west to the east (i.e., toward the FFS) and from the north-western and south-western tips of the FFS to its main depocenter, located a few km N-W of San Benedetto village (Fig. 1). Specifically, Cavinato et al. (2002) distinguished four unconformity-bounded units: Seq. 1, Meso-Cenozoic substratum, Seq. 2, Messinian, Seq. 3 Pliocene, and Seq. 4, Quaternary, separated by major unconformities A, B, and C, respectively (Fig. 1). The EW-trending seismic Line 1, crossing the depocenter of the basin, shows that Quaternary sediments, which here reach a maximum thickness of ~700 m, have not been significantly affected by tectonic deformation or sedimentary unconformities (Cavinato et al., 2002) (Fig. 1). During the past decades, several cores were drilled in the Fucino semi-graben basin for scientific and geotechnical purposes. So far, the 200 m-long GeoLazio core is the deepest borehole in the Fucino plain (GL in Fig. 1), but only very few data is available on its geochronological and stratigraphical aspects (Follieri et al., 1986; 1991; Giaccio et al., 2015b).

3. Material and methods

3.1. Drilling site selection strategy and procedure

The general semi-graben architecture of the Fucino Basin (Line 1, Fig. 1) was taken into account when selecting a new drilling site characterized by a lower sedimentation rate with respect to F1-F3 (~0.45 mm/yr in average, Giaccio et al., 2017; Mannella et al., 2019), i.e., potentially yielding older sediments to a relatively shallow depth. The respective site was located ~1 km east of the F1-F3 site (42°00'07"N, 13°32'19"E), in between the GeoLazio and SP cores (Fig. 1), both characterized by mean sedimentation rate of ca. 0.2 mm/yr (Giaccio et al., 2015b; 2017). **In order to recover a sedimentary succession as complete as possible, two parallel cores were recovered at the same drilling site in two boreholes, F4 and F5, ca. 3 m apart.** The first hole (F4) reached a field depth of 87.00 m and the second hole (F5) a depth of 87.75 m. Individual core sections had a length of 1.5 m, and both holes were drilled with an overlap of 75 cm between the respective runs, **thus ensuring that any possible gap in-between two consecutive core sections of the F4 core series was likely recovered in the middle of core section of the F5 core series, and vice versa (Fig. 2).** Samples from core catchers were taken directly in the field, whereas the rest of the core was stored in a dark and cool place for further analyses.

3.2. Downhole logging

Geophysical downhole logging data including natural gamma radiation (spectral gamma ray), magnetic susceptibility, resistivity, temperature, acoustic velocity, acoustic borehole televiewer, and borehole diameter and dip (borehole and strata) were measured in hole F4. Spectral gamma ray was logged first through the drill pipe and is the depth reference for all following runs. All other runs were performed under open hole condition. For that, the drill pipe was tripped out up to 67 m before logging the above-mentioned parameters separately. After finishing the logging of the interval ~80 m to 67 m, the drill pipe was pulled out to 1.5 m and the upper section was logged.

150 **3.3. Core processing, XRF scanning and composite F4-F5 record**

151 Sediment cores were split lengthwise and their lithology described at the Institute of Geology and Mineralogy
152 of the University of Cologne (Germany). Immediately after core opening, one of the core halves was scanned
153 for high-resolution images with a line-scan camera mounted on an ITRAX X-ray fluorescence (XRF) scanner
154 (Cox Analytical Systems, Sweden). XRF scans on split core halves were made using a chromium tube set at
155 55 kV and 30 mA with a dwell time of 10 s and a step-size of 2.5 mm. Data processing was performed with
156 the QSpec 6.5 software (Cox Analytical, Sweden) and data are expressed in counts per second, averaged at 25
157 cm intervals. Optical information derived from high-resolution line-scan imaging and XRF data were used for
158 correlating the individual, overlapping core segments from sites F4 and F5 to create a composite core (Fig. 2).
159 **Among homologous stratigraphic intervals documented in both F4 and F5 cores, we systematically selected**
160 **the more expanded one, which results in a total length of F4-F5 composite core that exceeds the depth of the**
161 **individual boreholes.** Sections that were obviously disturbed by the coring process were excluded from the
162 core composite or marked as not relevant for high-resolution analyses. If unambiguous core correlation was
163 not possible due to non-overlapping sections or larger disturbed sections, the field depth of the cores and the
164 length of the core catcher were taken as measures to continue the core composition downward. The length of
165 the resulting core composite, 98.11 m composite depth (mcd), exceeds the drilling field depth by 10.36 m,
166 which is partly due to core expansion and degassing after core recovery and **to the difference in the thickness**
167 **of homologous stratigraphic intervals documented in the F4 and F5 core sections selected for the composite**
168 **F4-F5 core.**

169
170 **3.4. Palaeomagnetic analyses**

171 For palaeomagnetic analyses the natural remanent magnetisation (NRM) of the core halves was measured
172 consecutively in 1 cm spacing by a cryogenic magnetometer (760 SRM-RF-SQUID; 2G Enterprise, USA)
173 with an embedded alternating field demagnetizer at the palaeomagnetic laboratory Grubenhagen of the Leibniz
174 Institute for Applied Geophysics (LIAG; Hannover, Germany). Subsequent progressive alternating field (AF)
175 demagnetization in four equally sized steps up to 16 mT. These measurements allow for a first evaluation of
176 the quality of the magnetic signal. The inclination values measured after the 16 mT demagnetisation step were
177 used to show downcore variations of the direction of the palaeomagnetic field. The inclination data of core
178 sections showing drilling induced disturbances were excluded from the interpretation, as well as the suspicious
179 values gained from the top and the bottom of drill core segments. Since core measurements integrate the signal
180 over approximately 12 cm, drilling induced disturbances influence the data of not affected core sections.
181 Thereby, data gaps exceed the actual disturbed sections of the core. The magnetic susceptibility (MS) of the
182 core halves was determined in 1 cm spacing using a 14 cm loop sensor and a VSFM control unite by Magnon
183 GmbH (Dassel, Germany).

184
185 **3.5. Tephrochronological analyses**

186 **3.5.1. Tephrostratigraphy and major element composition**

187 Major and minor oxide element compositions were determined on micro-pumice fragments and/or glass shards
188 of eleven selected tephra layers (Table 1) distributed along the F4-F5 succession as shown in Figure 2c. The
189 individual layers were labelled using an alphanumeric code that identified the hole (i.e., F4 or F5), the
190 progressive number of the section core (from 1 to 58) and the depth in cm of the top and bottom of the layer
191 in the ~150 cm-long core section (see second column in Table 1). Then, labels were simplified using the
192 criterion previously proposed for the F1-F3 core (Giaccio et al., 2017), i.e., the tephra have been labelled as
193 Tephra Fucino (TF) followed by a sequential number indicating the relative stratigraphic position of each
194 tephra, with TF-1 being the uppermost layer (Table 1).

195
196
197

Table 1: Analysed tephra layers from core F4-F5.

Fucino tephra	Sampling code	Bottom mcd	Thickness (cm)	Main lithological features	Source
TF-4	F5-8 77-93	10.57	15.50	Darkish coarse ash made of dense blackish porphyritic scoria including crystals of leucite, pyroxene and dark mica, also occurring as abundant loose clasts. Accessory lithic made of lava and holocrystalline clasts also occur.	Colli Albani
TF-5	F5-8 148-154	11.13	~6*	Darkish coarse ash made of dense blackish porphyritic scoria including crystals of leucite, pyroxene and dark mica, also occurring as abundant loose clasts. Accessory lithic made of lava and holocrystalline clast also occur.	Colli Albani
TF-7	F5-10 147-149	14.14	2.00	Greyish medium ash made of whitish-transparent micro-pumices associated with dense brownish glass shards with abundant loose crystals of large sanidine and black mica.	Ischia
TF-8	F5-12 90-95	17.15	4.50	Darkish ash made of blackish poorly vesicular scoria associated to scarce crystals of leucite and clinopyroxene.	Colli Albani
TF-12	F5-15 90-91	21.53	1.00	Greyish to dark yellow, fine grained ash with whitish-transparent micropumices and glass shards. Stretched/elongated vesicles, only very few loose crystals of sanidine, black mica and pyroxene.	Campi Flegrei-CVZ
TF-17	F5-20 89-91	29.64	2.00	Fine to coarse grained, greyish ash with 1) greyish dark vesicular scoria; 2) brownish and transparent glass shards and micropumice; 3) coarse, (rounded) whitish and greyish pumice, with loose sanidine, clinopyroxene, and amphibole crystals	Campi Flegrei-CVZ
TF-62	F4-39 90-100	60.60	10.00	Darkish coarse ash consisting of 1) greyish dark vesicular scoria; 2) brownish and transparent glass shards and micropumice; 3) coarse, (rounded) whitish and greyish pumice, with loose sanidine, clinopyroxene, and amphibole crystals.	Sabatini
TF-85	F5-49 74-88	80.52	13.25	Darkish medium-coarse ash made of both black porphyritic leucite-bearing scoriae and aphyric highly vesicular black scoriae, along with abundant crystals of leucite and dark mica and lithics. Toward the top, the ash becomes finer.	Colli Albani
TF-117	F5-57 0-7	95.13	7.00	Darkish fine ash made of black porphyritic leucite-bearing scoriae associated with free crystals of leucite and lithics. Toward the top, the sediment evolves into a coarse ash made of blackish vesicular porphyritic scoriae along with leucite and lithics.	Colli Albani
TF-118	F5-57 16-23	95.29	7.50	Darkish fine ash made of black porphyritic scoriae along with abundant free crystals of leucite and minor lithics.	Colli Albani
TF-126	F5-58 64- 66	97.24	2.00	Light-grey medium ash made of highly vesicular white pumices associated with crystals of sanidine, plagioclase, dark mica and opaques and glass shards and minor lithics. Toward the top, the sediment turns to a dark grey-blackish medium ash.	Vulsini

199 *Base of tephra inside of the core-catcher, not in composite depth.

200

201

202

203

204

205

206

207

208

209

210

211

212

213

214

215

216

217

In addition, in order to improve the available reference datasets for robust geochemical comparisons and for identifying the volcanic source of the Fucino tephra layers, **we are performing new glass chemical analyses of the main proximal volcanic units of Latium and Roccamonfina volcanoes, which are the main sources of the Fucino Middle Pleistocene tephra.** Specifically, **based on the estimated ages of the F4-F5 tephras investigated in this study**, glass shards and micropumices of pyroclastic fall and flow units from the Castel Broco eruption, Vulsini Volcanic District (e.g. Palladino et al., 2010), the Tufo Giallo di Sacrofano eruption, Sabatini Volcanic District (Sottili et al., 2010) and the layer R94-30C, from Tiber River MIS 11 aggradational successions (Marra et al., 2016), were analysed **and are presented in this study.**

Polishing and carbon coating of epoxy pucks were performed for electron microprobe analyzer wavelength dispersive spectroscopy (EPMA-WDS) analysis at the Istituto di Geologia Ambientale e Geoingegneria of the Italian National Research Council (IGAG-CNR, Rome), at the Institute of Geology and Mineralogy of the University of Cologne (IGM-UC, Germany) and at the Geoforschungszentrum (GFZ), Potsdam (Germany). At IGAG-CNR, geochemical analyses of individual glass shards were performed using a Cameca SX50 EPMA equipped with a five-wavelength dispersive spectrometer, calibrated and set to the same operating conditions as in previous studies (Giaccio et al., 2017). At IGM-UC, individual glass shards and reference standards were measured using a JEOL JXA-8900RL EPMA equipped with a five-wavelength dispersive spectrometer, which

218 was set to 12 keV accelerating voltage, 6 nA beam current, and 5 μm beam diameter. Detailed settings such as
219 counting times, measuring order, and reference materials used for calibration are given along with the
220 supplementary material. At the GFZ, major-element compositions of single glass shards were determined using
221 a JEOL JXA8500F EPMA. The instrument was set at an accelerating voltage of 15 kV, a 10 nA beam current,
222 and a 3–10 μm beam with count times of 20 s for the elements Mg, P, Cl, Ti, Mn, and Fe, and 10 s for F, Na,
223 Al, Si, K, and Ca. A range of MPI-DING reference glasses including GOR128-G (komatiite), ATHO-G
224 (rhyolite) and StHs6/80 (andesite) (Jochum et al., 2006) as well as natural Lipari obsidian (Hunt and Hill,
225 1996; Kuehn et al., 2011) were employed as secondary glass standards in order to maintain inter-laboratory
226 consistency of analytical data.

227 Geochemical analyses yielding analytical totals <93 wt.% were rejected, whereas all analyses with higher
228 totals were normalized to 100% on a LOI-free basis, excluding volatiles (Cl, SO₃, and F). Glass shards and
229 micropumices were classified according to their geochemical composition using total alkali vs. silica (TAS)
230 diagrams (Le Bas et al., 1986).

231

232 3.5.2. ⁴⁰Ar/³⁹Ar geochronology

233 ⁴⁰Ar/³⁹Ar geochronology was performed at the Laboratoire des Sciences du Climat et de l'Environnement
234 (CNRS-LSCE; Gif Sur Yvette, France). Tephra TF-126 (sample code F5-58 64-63; 97.24 m depth) was sieved
235 and subsequently 25 pristine sanidine crystals were picked from the 300 μm to 400 μm fraction. These crystals
236 were irradiated 2 hours in the Cd-lined, in-core CLICIT facility of the Oregon State University TRIGA reactor.
237 After irradiation, 15 crystals were individually loaded in a copper sample holder and put into a double vacuum
238 Cleartran window. Each crystal was then fused using a Synrad CO₂ laser at 15% of nominal power (~25 Watts).
239 The extracted gas was purified for 10 min by two hot GP 110 and two GP 10 getters (ZrAl). Argon isotopes
240 (³⁶Ar, ³⁷Ar, ³⁸Ar, ³⁹Ar and ⁴⁰Ar) were analysed by mass spectrometry using a VG5400 equipped with an
241 electron multiplier Balzers 217 SEV SEN coupled to an ion counter. The neutron fluence J value for each
242 sample was calculated using co-irradiated Alder Creek Sanidine (ACs-2 hereafter) standard with an age of
243 1.1891Ma (Niespolo et al., 2017) and the total decay constant of Renne et al. (2011). The J-value computed
244 from standard grains is $0.00053001 \pm 0.00000159$. Mass discrimination was estimated by analysis of Air
245 pipette throughout the analytical period, and was relative to a ⁴⁰Ar/³⁶Ar ratio of 298.56 (Lee et al., 2006).
246 Procedural blank measurements are computed after every two or three unknowns, depending on the beam
247 measured. For 10 min static blank, typical backgrounds are about $2.0\text{-}3.0 \cdot 10^{-17}$ and 5.0 to $6.0 \cdot 10^{-19}$ mol for ⁴⁰Ar
248 and ³⁶Ar, respectively. The precision and accuracy of the mass discrimination correction was monitored by
249 weekly measurements of air argon of various beam sizes.

250 For a consistent comparison of geochronological data, where possible (i.e., when monitor constant used is
251 known and declared), all ⁴⁰Ar/³⁹Ar ages used from the literature have been recalculated relative to an age of
252 1.1891 Ma for the Alder Creek sanidine monitor standard (Niespolo et al., 2017), with the uncertainties
253 expressed at 2 σ .

254

255 4. Results

256 4.1. Borehole data

257 Gamma ray logging data show a trend towards lower values from the bottom to the top, and the development
258 from shorter to longer periods from the base to the borehole top (Fig. 3b). While in the lower part several
259 quasi-cyclic **alternations** with a period around 5 m can be seen in the gamma ray data, two much longer quasi-
260 cycles from ~38-22 m and from ~22 m to the top are especially prominent. This ~20 m cyclicity can be seen
261 also further down in the record (Fig. 3b). Cyclic behaviour can be visualized in a wavelet analysis plot using
262 the 'biwavelet' R package (Gouhier et al., 2018; R Core Team, 2017), clearly showing the trend of longer
263 periods towards the top (supplementary Fig. S1). The seemingly strong cyclicity at ~35 m is the result of a
264 single peak in the data (see Figs. 2b and S1). The magnetic susceptibility shows various peaks from a base
265 line, but the log₁₀ of the magnetic susceptibility emphasizes a minor variability characterised by a quite regular
266 cyclicity, which appears coherent with that depicted by gamma ray (Fig. 3a).

267

268 4.2. Lithology and XRF scanning calcium counts of the F4-F5 composite core

269 The ~98 m-long F4-F5 core composite is mainly composed of grey-whitish lacustrine calcareous marl, with a
270 variable proportion of darkish clay. Starting from the depth of ~60 m, tephra layers become particularly
271 frequent and thick (up to 15-20 cm), and are often surmounted by dm-thick intervals made of volcanoclastic
272 material, likely deriving from the immediate reworking of tephra fallout in lake catchment.

273 Calcium represents one of the major element components of the sediments and shows large variations in XRF
274 counts ($0.15\text{-}4.60 \times 10^6$ cps) (Fig. 3e). Calcium has a polymodal statistical distribution, which can be divided
275 in seven, partially overlapping, normally distributed populations (Fig. 3e). A broad population of intermediate
276 values ($\mu \pm 2\sigma$: 2.30 ± 1.25) separates two groups consisting of three populations each and clustering in the
277 high ($\mu \pm 2\sigma$: 4.30 ± 0.30 ; 3.65 ± 0.50 ; 3.10 ± 0.35) and in the low ($\mu \pm 2\sigma$: 2.00 ± 0.22 ; 1.65 ± 0.30 ; $1.15 \pm$
278 0.60) range of Ca counts, respectively. These two clusters depict five intervals characterized by prevailing high
279 Ca counts intervened with four intervals with prevailing low Ca counts along the succession (Fig. 3e). The
280 thickness of intervals with prevailing high Ca counts ranges between 4.85 and 11.80 m, while intervals with
281 prevailing low Ca counts are thicker and range between 10.48 and 15.18 m in thickness.

282

283 **4.4. Palaeomagnetic data**

284 The palaeomagnetic data show normal direction with relative steep dipping inclination values (Fig. 3d).
285 Because of the rotation movement during the drilling process, the cores are not oriented for the North direction
286 and the declination cannot be taken into account. Gaps in the dataset arise from drilling induced disturbances,
287 which have destroyed the primary direction recorded in the sediment. After cleaning the data set, conspicuous
288 data occur around 13 mcd, 25 mcd, and 39 mcd. These sections are characterized by reversed inclination values
289 or flat dipping normal inclination values. In contrast to the data from drilling induced disturbances, which
290 show similar features, these changes in inclination are similarly recorded in both cores, F4 and F5. The MS of
291 the core material was used for determination of the relative palaeointensity (RPI) by normalizing the remanent
292 magnetization measured after the 12 mT AF demagnetization step by the MS (Tauxe, 1993). Because of very
293 low MS values ($< 15 \cdot 10^{-6}$ SI) of large parts of the cores a reliable calculation of the RPI was not possible by
294 this method.

295

296 **4.5. Tephra lithology and glass composition**

297 A total of ~130 visible tephra layers were identified in the F4-F5 composite profile during core inspection. The
298 thickness and main lithological features of the eleven investigated and described here tephra are summarized
299 in Table 1. Full glass compositions are provided in supplementary dataset 2 (SD 1), while their classification
300 according to the total alkali *versus* silica diagram (TAS, Le Bas et al., 1986) is shown in Figure 3a.

301 In the TAS diagram the analysed tephra layers cluster in two different compositional groups (CG), represented
302 by K-fooidites of CG1, which includes six layers (TF-4, TF-5, TF-8, TF-85, TF TF-116, and TF-117), and
303 potassic trachytes-phonolites to tephriphonolites and phonotephrites of CG2, which includes five other tephra
304 layers (TF-7, TF-12, TF-17, TF-62, and TF-126) (Fig. 4a).

305

306 **4.6. $^{40}\text{Ar}/^{39}\text{Ar}$ age of TF-126**

307 Full analytical details for individual crystals are given in the supplementary dataset 2 (SD 2) and presented in
308 Figure 4 as a probability diagram with the associated inverse isochron. Individual crystal age uncertainties are
309 given at 1σ level and weighted mean age uncertainties are quoted at 2σ level. After excluding three crystals
310 older than the main crystal age population, the remaining twelve crystals have equivalent ages within
311 uncertainty (Fig. 4) giving a meaningful weighted mean age of 424.3 ± 3.2 ka (MSWD = 1.16, P = 0.7; Fig.
312 4). This age is undistinguishable within uncertainty from the inverse isochron age (i.e., 422.8 ± 3.8 ka (MSWD
313 = 0.87). The $^{40}\text{Ar}/^{36}\text{Ar}$ initial intercept is identical within uncertainty to the atmospheric one (see SD 2),
314 excluding an excess argon component. Therefore, the age of 424.3 ± 3.2 ka (2σ) is considered as the age of
315 the eruption and deposition of tephra TF-126 hereafter.

316

317 **5. Discussion**

318 **5.1. Palaeoclimate and preliminary chronological framework for F4-F5**

319 The variability of Ca content in Fucino lake sediments is mainly related to variations in bio-mediated
320 precipitation of endogenic calcite, the precipitation of which depends on the lake's primary productivity, in
321 turn related to temperature and hydrology (e.g., Mannella et al., 2019). Based on the well constrained
322 tephrochronology available for the F1-F3 succession (Fig. 3g), fluctuations in the Ca XRF profile have been
323 demonstrated to express the glacial-interglacial and sub-orbital climatic variability of the last ~190 kyr, with
324 high Ca during warm MIS 5 and MIS 1, and lower Ca during the cold MIS 6 and MIS 4-MIS 2 (Mannella et
325 al., 2019) (Fig. 3f).

326 The general pattern of the major fluctuations of the Ca XRF curve recorded in the upper 35 mcd of the F4-F5
327 succession replicates the Ca XRF profile of the entire F1-F3 core, indicating that the two stratigraphic intervals
328 span the same temporal interval. With the exception of some sharp and prominent spikes, clearly related to
329 thick tephra layers, gamma ray and magnetic susceptibility signals of the upper 35 mcd of core F4-F5 fluctuate
330 coherently with Ca counts (Fig. 3a-b). This suggests they can be considered as further proxies of the glacial-
331 interglacial cyclicity. Indeed, low gamma ray and magnetic susceptibility are consistent with the low detrital
332 input during warm MISs, while high levels of these parameters indicate a high detrital input consistent with
333 colder and drier climatic conditions of the cold MISs.

334 The overlap of the upper 35 mcd of the F4-F5 core with the 83 m-long F1-F3 core, i.e., the last ~190 kyr
335 indicates a sedimentation rate of ~0.2 mm/yr for F4-F5, in line with estimates from the GL (Giaccio et al.,
336 2015b) and SP cores (Giaccio et al., 2017) located close by (Fig. 1). Additional confirmation is provided by
337 the tephrochronological study of the cores FUC-S5-6 (Di Roberto et al., 2018), where an average of ~0.13
338 mm/yr for the last 56 kyr has been shown. This lower sedimentation rate is in agreement with the position of
339 the FUC-S5-6 site, where the sedimentary wedge is expected to become thinner and the isochrones shallower
340 (Fig. 1).

341 Based on this coherent stratigraphic framework, the third, fourth, and fifth intervals with relatively high
342 concentration of Ca, and, conversely, low gamma ray and magnetic susceptibility, can be related to the MIS 7,
343 MIS 9 and MIS 11, respectively. The chronological framework is further supported by the direct $^{40}\text{Ar}/^{39}\text{Ar}$
344 dating of tephra TF-126, which provides a robust age constrain for the base of the fifth and last interval with
345 relatively high Ca content at $424.3.2 \pm 3.2$ ka (Fig. 3g), near the onset of MIS 11 at 424 ka based on the benthic
346 isotope stack (Lisiecki and Raymo, 2005) (Fig. 3g) and ~426 ka based on U/Th dating from the Chinese
347 speleothems (Chen et al., 2016). **Despite this strong chronological constrain, the general shape of the Ca profile**
348 **corresponding to the MIS 11 interval appears quite fragmentary with respect to a more regular trend expected**
349 **for this period, as, e.g., recorded in LR04 benthic record (Fig. 3h). This might be due to both significantly**
350 **changing in sedimentation rates and the occurrence of tephra layers (Fig. 3c), which are quite frequent and**
351 **thick in this stratigraphic interval, that results in strong disturbances of the Ca profile that mimic climatic**
352 **oscillations within MIS 11. Therefore, in order to have a reliable climatic expression of MIS 11, a detailed age**
353 **model need to be developed by removing all tephra layers; a procedure which is commonly done when dealing**
354 **with detailed paleoclimatic investigations (e.g., Mannella et al., 2019), but unnecessary for the purposes of this**
355 **paper. We can thus use the preliminary chronological framework deriving from the correlation of the F4-F5**
356 **with the LR04 benthic record (Fig. 4; Lisiecki and Raymo, 2005) for getting a first age estimation of the tephra**
357 **in the lower part (35-98 mcd) of the F4-F5 core. This provides useful, though approximate, chronological**
358 **constraints for circumscribing the time interval to be consider to identify the potential equivalents of the Fucino**
359 **tephra layers (Fig. 3c). For this purpose, we considered the position of the F4-F5 tephras in Ca profile to**
360 **evaluate their climatostratigraphic context within the record of the LR04 benthic stack, and thus to estimate**
361 **their age according to LR04 chronology assuming a conservative uncertainty of ca. ± 5 ka (Fig. 3g).**

362

363 **5.2. Palaeomagnetic data of F4-F5**

364 In comparison to the $\sim 58^\circ$ inclination of today's earth magnetic field in the Fucino Basin, the determined
365 inclination values of the palaeomagnetic field of the sediments from F4-F5 cores are frequently too steep (Fig.
366 3d). The deviation may arise from slight deformations of the material during the coring process, just as by
367 considering the inclination of the 16 mT AF step instead of evaluating the characteristic remanent
368 magnetisation (ChRM). However, downcore changes of the palaeomagnetic field show sections with
369 conspicuous values around 13 mcp, 25 mcp, and 39 mcp. According to the age constrains provided by
370 tephrochronology, these features coincide with the positions expected for the geomagnetic excursions
371 Laschamp (40-41 ka), Blake ($\sim 120 \pm 12$ ka), and Iceland Basin (189-192 ka), respectively (Channell, 2006;
372 Channell 2014; Singer et al., 2014; Vasquez and Lidzbarski 2012). This result suggests the Fucino Basin to
373 host an outstanding magnetic record and justifies the planned very time-consuming detailed study of discrete
374 samples, necessary to consider the ChRM.
375

376 **5.3. Volcanic sources of tephra layers from core F4-F5**

377 The Fucino Basin is located at a relatively short distance from the peri-Tyrrhenian and the insular Quaternary
378 Italian volcanic centres (i.e., ~ 100 km to some hundreds of km; Fig. 1) that were subjected to intense and
379 frequent explosive activity during the Quaternary (e.g. Peccerillo, 2017). Hence, these volcanic centres
380 represent the most likely sources for the Fucino tephra layers. The geochemical composition of CG1 (Fig. 4a)
381 tephra layers is unusual within the framework of the Italian Quaternary volcanism since large explosive
382 eruptions fed by K-foiiditic magma were rare and characteristic of only few volcanic centres (e.g. Peccerillo,
383 2017). Among these, the Colli Albani volcanic district was the most productive source of foiditic distal tephra
384 in Central Mediterranean area (e.g. Giaccio et al., 2013a; Giaccio et al., 2014; Giaccio et al., 2017; Leicher et
385 al., 2016; Petrosino et al., 2014b).

386 The glass geochemical compositions of CG2 (potassic trachytes-phonolites to tephriphonolites and
387 phonotephrites) tephra layers are instead shared by a number of volcanic districts and centres ranging from the
388 northern Latium to the Campanian regions (e.g., Peccerillo, 2017) (Fig. 1), making the identification of their
389 specific volcanic source challenging. However, the CaO/FeO vs Cl diagram (Giaccio et al., 2017) can help to
390 discriminate between their different sources (Fig. 4b). Thus, layer TF-7 can be referred to Ischia, layers TF-
391 12/-17 to Campi Flegrei, and layer TF-126 to the Latium volcanoes, including Vico, Vulcini and Sabatini (Fig.
392 4b). The source of the remaining tephra TF-62 is more complicated to define, as its composition falls at the
393 boundary between the Roccamonfina >450 ka and Latium volcano fields (Fig. 4b). However, based on the
394 stratigraphic position of TF-62 within late MIS 9 (~ 280 -300 ka, Fig. 3g-h), it can be better ascribed to the
395 Latium volcanoes than to Roccamonfina, as, at the current state of knowledge, the products from
396 Roccamonfina <450 ka have a distinctly higher content of Cl and a lower CaO/FeO ratio (Fig. 4b).
397 Furthermore, at the same content of Cl, tephra TF-62 shows a relatively high and wide variability of the
398 CaO/FeO ratio (1.0 to 1.5, Fig. 4b), which, among the Latium volcanoes, is distinctive of the products from
399 the Sabatini Volcanic District. Therefore, layer TF-62 can be more likely referred to the Sabatini activity. A
400 summary of the source attribution of all investigated tephra is reported in Table 1.
401

402 **5.4. Individual tephra correlation**

403 *5.4.1. Tephra layers between 0-35 mcd of core F4-F5, equalling 0-83 mcd of the F1-F3 core*

404 A total of six chemically analysed tephra layers occurring within the upper 35 mcd in the new F4-F5 core can
405 be directly linked to already identified tephra layers from the F1-F3 core. These include tephras TF-4, TF-5,
406 TF-7, TF-8, TF-12 and TF17 (Giaccio et al., 2017), which have been allocated to volcanic sources from the
407 Campanian and Roman areas and which are described in the following in more detail.
408

409 5.4.1.1. Tephra from Colli Albani (GC1)

410 **F5-8 77-92 (10.56 mcd; TF-4) and F5-8 148-154 (11.13 mcd; TF-5)** – these two tephra layers, belonging to
411 the K-foiidite CG1 tephra group that is attributed to the Colli Albani activity, share similar lithological features
412 (Table 1) and heterogeneous glass compositions within the foidite field (Fig. 4a). Comparable lithological and
413 geochemical features have been found in layers TF-4 and TF-5 in the F1-F3 record (Fig. 6a-b), which were

414 correlated by Giaccio et al. (2017) to the Albano 7 (35.8 ± 1.2 ka) and Albano 5 units (38.7 ± 1.6 ka, Freda et
415 al., 2006; Giaccio et al., 2009; 2017; Mannella et al., 2019), respectively (Fig. 3f). In addition, the
416 climatostratigraphic position of the two foiditic layers in F4-F5 within MIS 3 is similar to that of TF-4 and TF-
417 5 (Fig. 3d-e), hence strongly supporting their correlations with TF-5/Albano 7 and TF-4/Albano 5. In the F4-
418 F5 record, TF-4 is characterized by two coarse ~ 4.2 and 7.2 cm-thick levels separated by 5 cm of fine ash and
419 lacustrine sediments, a lithological feature that is not observed in F1-F3. However, a similar lithological
420 bifurcation of the tephra related to the most recent activity of the Albano maar, has been found in cores FUC-
421 S5-6 (Di Roberto et al., 2018). The two levels of coarse-grained ash were interpreted by the authors as separate
422 units and correlated to the last two eruptions of Albano maar, namely Albano 7 and 6. However, in the eastern
423 sector of Colli Albani, where the mid-distal occurrences of the Albano eruptions are well documented, only
424 four fallout units, related to Albano 1, 3, 5, and 7 can be recognised (Giaccio et al., 2007). The lack of the
425 Albano units 2, 4, and 6 in the eastern, mid-distal sectors of the volcano, indicates the moderate intensity of
426 the eruptions and their restricted dispersal, with respect to the widespread Albano units 1, 3, 5, and 7. Thus, it
427 is rather unlikely that tephra of the Albano 6 eruption has reached the Fucino Basin and would show
428 comparable thicknesses and grain sizes as tephra from the largest Albano 7 eruption. Therefore, the two coarser
429 sub-layers forming TF-4 can be more likely correlated to the two main fallout sub-units (DU4b and DU4c),
430 that form the succession of the Albano 7 unit in mid-distal area (Giaccio et al., 2007). Alternatively, they could
431 be the result of a basal fallout (basal sub-layer) that was followed by immediate reworking of primary deposits
432 (upper sub-layer).

433

434 **F5-12 90-95 (TF-8, 17.16 mcd)** – the foiditic composition of F5-12 90-95 is distinctly more homogenous
435 compared to the above discussed TF-4 and TF-5 tephra layers (Fig. 6c). This geochemical feature is
436 comparable with the glass composition of tephra layer TF-8 in core F1-F3 (Fig. 6c), which is correlated to the
437 Albano 3 unit and dated between 68.7 ± 2.2 ka and 72.5 ± 3.2 ka (Freda et al., 2006; Giaccio et al., 2009). The
438 correlation of F5-12 90-95 with TF-8/Albano 3 is also supported by the similar climatostratigraphic position
439 that the two tephra have in the respective records at the end of the MIS 5 period (Fig. 3e-f).

440

441 5.4.1.2. Tephra from Ischia (GC2)

442 **F5-10 147-149 (14.14 mcd; TF-7)** – The ages of this Ischia tephra is constrained by the overlying TF-5 and
443 underlying TF-8 tephra between ~ 40 ka and ~ 70 ka, (Fig. 5f-g). The trachytic glass composition of F5-10 147-
444 149 matches that of tephra TF-7 (Fig. 7a) which is in a similar climatostratigraphic position within MIS 4 in
445 composite core F1-F3 (Fig. 3d-e) and directly $^{40}\text{Ar}/^{39}\text{Ar}$ dated at 55.9 ± 1.0 ka (Giaccio et al., 2017). TF-7 has
446 been correlated to the marine Y-7 tephra (Giaccio et al., 2017), a widespread Mediterranean marker tephra
447 (Tomlinson et al. 2014), deriving from the Ischia eruption of the Monte Epomeo Green Tuff ($^{40}\text{Ar}/^{39}\text{Ar}$ age:
448 55.0 ± 4.0 ka, Sbrana and Toccaceli, 2011). Furthermore, the occurrence of the Y-7 tephra is also recorded in
449 Fucino cores FUC-S5-6 (Di Roberto et al., 2018).

450

451 5.4.1.3. Tephra from Campi Flegrei (GC2)

452 **F5-15 90-91 (21.53 mcd; TF-12)** – this tephra is located in a climatostratigraphic position similar to tephra
453 layers TF-12 and TF-13 of the F1-F3 record, i.e., close to the onset of an abrupt increase in Ca content occurring
454 in the middle part of MIS 5 (Fig. 3e-f). TF-12 and TF-13 have been correlated to the widespread marine tephtras
455 X-5 and X-6, respectively (Giaccio et al., 2017). Although X-5 and X-6 were generated by two, temporally
456 closely spaced eruptions of the same volcanic source – likely palaeo-Campi Flegrei or the Campanian Volcanic
457 Zone – as shown in Figure 6b, they are quite well distinguishable solely on the basis of major element
458 composition. The geochemical comparison with both layers (Fig. 7b) suggests that tephra F5-15 90-91 matches
459 best the composition of TF-12/X-5. The X-5 tephra has been also identified as POP3 equivalent in the Sulmona
460 lacustrine succession in central Italy where it is $^{40}\text{Ar}/^{39}\text{Ar}$ dated at 105.6 ± 3.0 ka (Giaccio et al., 2012b). A
461 newer and more precise $^{40}\text{Ar}/^{39}\text{Ar}$ dating of X-5 at 105.5 ± 0.5 ka derives from the Tyrrhenian Sea (Petrosino
462 et al., 2016).

463 **F5-20 89-91 (29.65 mcd; TF-17)** – on the basis of climatostratigraphic correlation between the F4-F5 and the
464 chronologically well constrained F1-F3 record, tephra F5-20 89-91 can be placed into the MIS 6 period (Fig.
465 3e). Geochemically, it is characterised by a wide composition with SiO₂ content ranging between 48 and 61
466 wt%. In the F1-F3 succession, the only Campi Flegrei tephra showing the same geochemical variability and
467 climatostratigraphic position is TF-17 (Figs. 2e-f and 6c). TF-17 has been ⁴⁰Ar/³⁹Ar dated at 158.3 ± 3.0 ka
468 (Giaccio et al., 2017). Amato et al. (2018), on the basis of geochronological and geochemical data, identified
469 TF-17 as the distal counterpart of the Taurano Ignimbrite from the Campanian Volcanic Zone (CVZ), which
470 has an ⁴⁰Ar/³⁹Ar age of 160.1 ± 2.0 ka (De Vivo et al., 2001).

471 472 *5.4.2. Tephra layers in the newly explored interval 35-98 mcd of core F4-F5*

473 Five out of ~110 visible tephra layers within the newly extended interval between 35-98 mcd of core F4-F5
474 have been chemically characterised and correlated with Roman volcanoes based on published and new glass
475 data from proximal tephra deposits.

476 477 *5.4.2.1. Tephra from Colli Albani (GC1)*

478 **F5-49 74-88/TF-85 (80.52 mcd), F5-57 0-7/TF-117 (95.13 mcd) and F5-57 18-22/TF-118 (95.29 mcd)** –
479 based on geochronological constraints – i.e., the tephrostratigraphic correlation between the successions of F4-
480 F5 and F1-F3, the general climatostratigraphic pattern of F4-F5, and the ⁴⁰Ar/³⁹Ar dating of the tephra TF-126
481 – and the typical foiditic glass composition tephra layers TF-85 (F5-49 74-88), TF-117 (F5-57 0-7) and TF-
482 118 (F5-57 18-22) can be related to activities of the Colli Albani volcanic district. Specifically, these layers
483 refer to the middle-late stage of the ‘Tuscolano-Artemisio’ (~561-351 ka, Karner et al., 2001) or ‘Vulcano
484 Laziale’ phase (Giordano et al., 2006). This phase is the most significant in terms of erupted volumes and
485 intensity of the Colli Albani eruptive history, and comprises several caldera-forming eruptions, the products
486 of which have been widely dispersed in the central-southern Apennines (Giaccio et al., 2013a; Giaccio et al.,
487 2013b; Giaccio et al., 2014; Petrosino et al., 2014b) and in the Balkans (Leicher et al., 2016). Furthermore,
488 tephra glasses from each one of the major units belonging to the Tuscolano-Artemisio phase, have a quite
489 distinctive major element composition, making their discrimination and identification unambiguous (Giaccio
490 et al., 2013a).

491 The significant thickness and the relatively coarse grain-size of TF-85 (Table 1) are consistent with a large
492 explosive eruption, which, based on the climatostratigraphic position of TF-85 in core F4-F5, occurred during
493 MIS 10, roughly between 350-375 ka (Fig. 3d-f). In this time-period was the Villa Senni eruption, the most
494 recent caldera-forming event of the Tuscolano-Artemisio phase, dated at 364.0 ± 4.0 (Marra et al., 2009) and
495 369 ± 4.2 ka (Marra et al., 2019). The major element glass composition of tephra TF-85 matches that of the
496 glassy scoria from the proximal Villa Senni unit and its distal equivalent tephra PAG-t4, from Paganica-San
497 Demetrio Basin, central Italy, dated to 368.0 ± 2.0 ka (Giaccio et al., 2012a) (Fig. 8a). TF-85 can be thus
498 confidentially correlated to the Villa Senni eruption.

499 Tephra TF-117 (95.13 mcd) is characterized by a noticeable thickness of 7 cm and a coarse grain-size,
500 suggesting again a large Colli Albani explosive eruption. Based on its climatostratigraphic position and being
501 located ~3 m above the ⁴⁰Ar/³⁹Ar dated TF-126, this eruption occurred early in MIS 11, at ~400-420 ka (Fig.
502 3d-f). The estimated high eruption magnitude and the supposed age of TF-117 are compatible with the
503 penultimate large eruption of the Tuscolano-Artemisio phase; i.e., the Pozzolane Nere eruption dated at 405 ±
504 2 ka (Marra et al., 2009). Comparisons of the geochemical composition of TF-117 with that of the proximal
505 Pozzolane Nere equivalents confirm the correlation (Fig. 8b). Specifically, the 2 cm-thick basal unit of TF-
506 117 (sample F5-57 5-7; Table 1) shows a more homogenous composition with respect to the more scattered
507 composition of the overlying, 5-cm-thick and coarser sub-unit (sample F5-57 0-5; Table 1), which matches
508 very well that of the basal Plinian fall-out of the Pozzolane Nere (Marra et al., 2009). Therefore, the basal,
509 finer and geochemically more homogeneous sub-layer of TF-117 (TF-117_{0.2}) can be related to the basal Plinian
510 fallout Pozzolane Nere, and consequently the uppermost, coarser and geochemically more scattered sub-layer

511 TF-117₂₋₇ should represent the co-ignimbrite ash fall. However, because of strong post-depositional,
512 zeolitization processes (Marra et al., 2009), no glass chemical data is currently available for the proximal
513 pyroclastic flow deposits of the Pozzolane Nere for directly compare with the composition of tephra TF-117₂₋₇.
514 The composition of the TF-117₂₋₇ thus provides the first geochemical data for the pyroclastic flow deposits
515 of the Pozzolane Nere eruption, which **in terms of erupted volume** represents the **main stage** of the eruption.
516 TF-118 layer (95.29 mcd) has a comparable thickness (ca. 7 cm) to that of TF-117/Pozzolane Nere (Table 1),
517 but its finer grain, which could be due to **either a** significantly smaller magnitude of the explosive event or a
518 different **shape and direction of the dispersion axis**. It is separated from the overlying TF-117/Pozzolane Nere
519 (95.13 m) by only 12 cm of lacustrine sediments (Fig. 3c; Table 1), indicating that TF-118 shortly preceded
520 the Pozzolane Nere eruption. Pereira et al. (2018) recognized a new Colli Albani eruption just below the
521 Pozzolane Nere units; the Fontana Ranuccio 2 fallout, dated at 407.1 ± 4.2 ka (2 σ analytical uncertainties) and
522 interpreted as a Pozzolane Nere precursor. Fontana Ranuccio 2 fallout is therefore a good candidate for
523 correlating with TF-118, immediately below the TF-117/Pozzolane Nere tephra, a hypothesis that is **quite well**
524 supported by its glass composition (Fig.7c). **However, as the geochemical matching is not perfect, especially**
525 **for SiO₂ content, the correlation of TF-118 with Fontana Ranuccio 2 has to be considered as a tentative.** The
526 age of this Pozzolane Nere precursor is statistically indistinguishable from the age of the Pozzolane Nere, but
527 it is slightly different in its geochemical composition (Pereira et al., 2018; Fig. 8c), making the discrimination
528 of these two sub-contemporaneous eruptions viable.

529 In summary, the stratigraphic order, the lithological and geochemical features and general climatostratigraphic
530 and geochronological settings available for the three foititic layers TF-85, TF-117 and TF-118 define an
531 overall coherent and robust framework supporting their correlation with Villa Senni, Pozzolane Nere, and,
532 **likely**, Fontana Ranuccio 2 eruptions from Colli Albano volcano, respectively.

533
534 5.4.2.2. Tephra from the Sabatini volcanic district (GC2)

535 **F4-39 90-100/TF-62 (59.89 mcd)** – by considering its relatively large thickness (10 cm), coarse grain-size
536 (Table 1) and phonolitic glass composition, tephra TF-62 likely derived from a large explosive eruption from
537 the Sabatini volcanic district. Layer TF-62 occurs in the late part of the MIS 9 period, roughly at 300-280 ka
538 (Fig. 3f). Thus, it is chronologically consistent with the early stages of the Sacrofano Caldera phase, which took
539 place in the eastern sector of the Sabatini Volcanic District (SVD) at ~300-200 ka, and the near-
540 contemporaneous Bracciano Caldera phase, which occurred in the central area of SDV at ~325-200 ka (Sottili
541 et al., 2010).

542 The Sacrofano Caldera phase is dominated by diffuse Strombolian and hydromagmatic activity and
543 subordinate Plinian to sub-Plinian events, among which the Tufo Giallo di Sacrofano (288.0 ± 2.0 ka, Sottili
544 et al., 2010) and the Magliano Romano Plinian fall (313.0 ± 2.0 ka, Sottili et al., 2010) stand out as the major,
545 caldera forming eruptions.

546 The Bracciano Caldera phase was similarly characterized by strombolian, effusive, and hydromagmatic
547 activity, but also by the occurrence of some large explosive events, including the main caldera forming
548 eruptions of the Tufo di Bracciano Unit (324.0 ± 2.0 ka, Pereira et al., 2017), the Tufo di Pizzo Prato ($251.0 \pm$
549 16.0 ka, Sottili et al., 2010), and the latest Tufo di Vigna di Valle (196.0 ± 7.0 ka, Sottili et al., 2010) pyroclastic
550 flow-forming eruptions.

551 The best candidate for a correlation of TF is the large caldera forming eruption of the Tufo Giallo di Sacrofano
552 (TGDS), as its large magnitude fit with the relatively thick and coarse TF-62 and its age is close to the estimated
553 age of TF-62 (~280-300 ka; Fig. 3g). In the TAS diagram and other selected bi-plots, the glass chemical
554 composition of TGDS shares with the predominant (~65% of the analysed glass particles), most evolved
555 component of the TF-62 the alkali and SiO₂ content (~15-16 wt% and 56-58 wt%), a peculiar high Al₂O₃
556 content (20.5-21.5 wt%) (Fig. 9a), and a very low MgO content (0.15 wt%) (Table S1). In summary, with the
557 exception of the K₂O/Na₂O ratio, which is higher in TGDS with respect to TF-62 (Table S1), the content of all
558 other major and minor elements of the most evolved component of the TF-62 matches very well the TGDS

559 glass composition (Table S1). Therefore, the TGDS is indicated as the most probable proximal counterpart for
560 TF-62, giving an age of 288.0 ± 2.0 ka to this latter.

561

562 5.4.2.3. Tephra from the Vulsini volcanic district (GC2)

563 **F5-58 64-66/TF-126 (97.24 mcd)** – the $^{40}\text{Ar}/^{39}\text{Ar}$ age directly determined on tephra TF-126 (424.3 ± 3.2 ka,
564 Fig. 4), restricts the chronological range of the potential equivalent to the narrow interval of ~ 421 - 428 ka.
565 Based on its phonolitic composition and the CaO/FeO vs Cl diagram either the Vulsini, Vico, or Sabatini
566 volcanic districts can be potential sources of this tephra (Fig. 5b).

567 The Southern Sabatini phase (~ 500 to ~ 400 ka, Marra et al., 2014) was the most intense one in terms of
568 explosivity and magnitude of the eruptive history of Sabatini Volcanic District (Sottili et al., 2004). However,
569 no significant eruption has been recognized so far between the Plinian Fall F dated to 449.0 ± 7.0 ka (Marra et
570 al., 2014) and the following minor activity of the San Abbondio Ash-lapilli Succession, dated to 391.0 ± 4.0 ka
571 (Marra et al., 2014). Therefore, at the present state of the knowledge, a Sabatini origin for TF-126 appears
572 unlikely.

573 The earliest activity of Vico volcano, the Vico Period I (Perini et al., 2004) of ~ 400 - 420 ka (Barberi et al.,
574 1994) was also characterized by an intense explosive activity and by the occurrence of two Plinian eruptions,
575 named Vico α and Vico β (Cioni, 1987; Laurenzi and Villa, 1987). Unfortunately, only whole-rock
576 geochemical composition are available for the proximal units of Vico Period I at present, which are not fully
577 suitable for a reliable chemical comparison with tephra glass composition. Glass geochemistry is however
578 available for some tephra attributed to Vico Period I found in distal settings of Rome area, Tuscany region,
579 Sulmona Basin and Lake Ohrid (Bigazzi et al., 1994; Marra et al., 2014; 2016; Regattieri et al., 2016; Kousis
580 et al., 2018), and that thus likely represent the main explosive eruptions of this Vico phase. All these studies
581 indicate that the most widespread tephra of Vico Period I are unusual with respect to the most common
582 compositions of the Latium ultrapotassic rocks (i.e., trachyte, phonolite, tephriphonolite), as they are
583 characterized by a trachytic-rhyolitic bimodal composition, with a distinctive rhyolitic component being often
584 the dominant or even the sole one. In combination with the slightly older age than Vico Period I, the lack of a
585 rhyolitic population in TF-126 would rule out Vico as a possible source of TF-126 tephra.

586 The **upper part of the** Bieadano Synthem of the Vulsini Volcanic District, spanning the late MIS 12-MIS 10
587 period, and thus encompassing the age of TF-126, comprises at least three Plinian falls. The Ponticello Pumices
588 (352.0 ± 4.0 ka), the Pumice Fallout 0 (381.0 ± 9.0 ka), and the Castel Broco eruptions (Palladino et al., 2010).
589 Of these, only Castel Broco is chronologically consistent with TF-126, although no direct age determination is
590 available for pyroclastic units of this eruption. Castel Broco deposits are in fact found below a **Vico α** , dated
591 to 419.0 ± 3.0 ka (Laurenzi and Villa, 1987), and above the Piano delle Selva Ignimbrite, which is substantially
592 younger than ~ 490 ka (Palladino et al., 2010 and references therein). The major element chemical composition
593 of glass from both Plinian and pyroclastic flow units of Castel Broco succession match quite well that of TF-
594 126 (Fig. 9b). Though the wide age range of Castel Broco eruption does not allow a precise chronological
595 confirmation, the chemical composition strongly supports the correlation of TF-126 with Castel Broco, which
596 thus could be indirectly, but precisely, dated at 424.3 ± 3.2 ka.

597 As far as the potential distal equivalents are concerned, the age of TF-126 is statistically indistinguishable from
598 those of the following three tephra: (i) R94-30C, from Roma costal area, which marks the glacial termination
599 V in MIS 12-MIS 11 aggradational successions of the Tiber River, yielding a $^{40}\text{Ar}/^{39}\text{Ar}$ age of 423.4 ± 5.0 ka
600 (Marra et al., 2016); (ii) OH-DP-1733, from Lake Ohrid succession, which is stratigraphically located at the
601 MIS 12-MIS 11 transition of the Lake Ohrid palaeoclimatic records, with a modelled age of 422.3 ± 6.1 ka
602 and attributed to the Roccamonfina volcano (Leicher et al., in review); and (iii) MOL 13, from Bojano Basin,
603 southern Italy, dated by $^{40}\text{Ar}/^{39}\text{Ar}$ method at 427.3 ± 6.0 ka and related to Rio Rava phase activity (550 - 358
604 ka; Rouchon et al., 2008) of the Roccamonfina volcano (Amato et al., 2014).

605 However, certain differences in glass composition do not support a correlation of the three Roman, Bojano and
606 Ohrid tephra, neither among them nor with TF-126 tephra (Fig. 9b). This highlights a quite complex framework

607 of the central Mediterranean tephrostratigraphy during the MIS 12-MIS 11 transition (cfr. Leicher et al., in
608 review), indicating the occurrence of several temporally closely spaced eruptions from multiple peri-
609 Tyrrhenian volcanic sources, including Vulcini (Castel Broco/TF-126), Roccamonfina (post-Rio Rava, MOL
610 13 and OH-DP-1733) and at least another currently undetermined volcano (R94-30C, Vico?).

611 **5.5. The composite Fucino tephra record and preliminary age model**

612 **5.5.1. F1-F3/F4-F5 composite tephra record spanning the last 430 kyr**

613 The recognition of tephra TF-4, TF-5, TF-7, TF-8, TF-12, and TF-17 in the F4-F5 record, shared with the
614 previously investigated core F1-F3, allows a robust synchronization of the two records along six tie points
615 (Fig. 10). Moreover, the high-resolution XRF Ca profiles of the F1-F3 and F4-5 successions enable further
616 refinement of the correlation using the high-frequency variability of this element as an aligning tool (Fig. 9),
617 **which allows us to transfer, on the basis of the tephra stratigraphic order and climatostratigraphic position, all**
618 **F4 tephra in F5 record, and vice versa (Fig. 10).** This results in a composite F1-F3/F4-F5 record of 134 tephra
619 that would make Fucino Basin the richest archive of the peri-Tyrrhenian explosive volcanism continuously
620 spanning over the last 430 kyr.

621 Significantly, the new F4-F5 composite record improves the general tephrostratigraphic framework, not only
622 for the previously unexplored temporal interval of ~190-430 ka (Fig. 11), but also for the interval spanning the
623 last 190 kyr (Fig. 10). Indeed, the combination of the F1-F3 and F4-F5 cores adds seven new tephra in the 190
624 ka-present interval that apparently were not documented in core F1-F3, because of either drilling issues and/or
625 the possible lenticular geometry of the tephra beds. Four of these new tephra layers are situated in a MIS 3-
626 MIS 4 interval between TF-7 (Y-7, ~56 ka) and TF-8 (~70 ka), one at the onset of MIS 5, just below TF-14
627 (Sabatini, 126.0 ± 1.0 ka), and two in MIS 6, preceding TF-17 (Taurano Ignimbrite, 159.4 ± 1.6 ka) (**Figs. 10**
628 **and 11**).

629 However, the major contribution of the F4-F5 record in building the new composite Fucino tephra record is
630 represented by its lowermost interval between 35-98 mcd. F4-F5 enables us to extend the Fucino record back
631 to 430 ka, with more than 100 tephra spanning the MIS 7-MIS 11 or 190-430 ka interval (Fig. 11). Indeed,
632 within the framework of the central Mediterranean tephrostratigraphy, the MIS 7-MIS 11 interval is among
633 the lesser documented and known. Many of the terrestrial or marine records of this region span either younger
634 (e.g., Monticchio: Wulf et al., 2004; 2012; San Gregorio Magno; Munno and Petrosino, 2007; Tyrrhenian Sea:
635 Paterno et al., 2008; Adriatic Sea: Bourne et al., 2010; Bourne et al., 2015; Ionian Sea; Insinga et al., 2014) or
636 older, and also discontinuous, intervals (Acerno Basin: Petrosino et al., 2014b; Mercure Basin: Giaccio et al.,
637 2014; Petrosino et al., 2014a; Sulmona Basin: Giaccio et al., 2015b). Furthermore, other long continuous
638 successions spanning the MIS 7-MIS 11 period are located too far from the highly productive peri-Tyrrhenian
639 volcanic sources (e.g., Lake Ohrid: Leicher et al., 2016; in review; Tenaghi Philippon: Vakhrameeva et al.,
640 2018; Vakhrameeva et al., 2019) for recording the bulk of their history and the wide gamma of their explosive
641 intensity, including eruptions of moderate magnitude. With ~110 tephra layers distributed in the MIS 7-MIS
642 11 interval, the composite F1-F3/F4-F5 record has thus the potential for filling the gap of knowledge for this
643 interval of the central Mediterranean tephrochronology.

644 **5.5.2. Preliminary age model for the F1-F3/F4-F5 composite record**

645 The directly $^{40}\text{Ar}/^{39}\text{Ar}$ dated tephra TF-126 (424.3 ± 3.2 ka, correlated to Castel Broco Plinian eruption from
646 Vulcini), and the ages transferred by geochemical fingerprinting from prominent eruptions of known age
647 (Pozzolane Nere precursor ~407 ka, Pozzolane Nere ~405 ka, Villa Senni ~368 ka and Tufo Giallo di
648 Sacrofano ~288 ka) provide a first chronological foundation for the MIS 7-MIS 11 period. Together with the
649 well-established chronology for the last 190 kyr (Giaccio et al., 2017; Mannella et al., 2019), this chronological
650 information allows us to develop a first age model for the entire F1-F3/F4-F5 Fucino composite record (Fig.
651 12). The resulting age-depth curve for the newly explored interval is consistent with that previously established
652 for the first 190 kyr, determined for core F1-F3 and now merged in the composite F1-F3/F4-F5 record (Fig.
653 12). This preliminary tephra-based age-model substantially refines and consolidates the initial chronology for
654 12). This preliminary tephra-based age-model substantially refines and consolidates the initial chronology for
655

656 the MIS 7-MIS 11 inferred from the palaeoenvironmental variability (Fig. 3), which appears fully coherent
657 with both orbital and millennial-scale climatic fluctuations of the MIS 11-MIS 7 period, as shown by the
658 comparison with the sea surface temperature fluctuations on the Iberian Margin (Rodrigues et al., 2017; Fig.
659 12). The same age-model is also consistent with the known chronology for the Laschamp (40-41 ka), Blake
660 (~120 +/- 12 ka), and Iceland Basin (189-192 ka) geomagnetic excursions, as preliminarily recognised in
661 Fucino sedimentary archive (Fig. 12). Future investigations of discrete samples will permit to verify the
662 occurrence of these geomagnetic excursions and likely contribute to detail their dynamics and age.

663 Though we are aware of its preliminary state, such a chronological framework of the Fucino composite record
664 is important for the forthcoming development of tephra and proxy investigations of Fucino cores, and,
665 consequently, for getting high-resolution and fully independently dated tephrochronological,
666 palaeoenvironmental and palaeomagnetic records.

667

668 **6. Summary and concluding remarks**

669 This paper presents the first results of ongoing multiproxy investigations on a new ~98 m-long sediment core
670 (F4-F5) retrieved from the Fucino Basin, central Italy. Concordant palaeoenvironmental (calcium XRF
671 scanning data from core F4-F5 and gamma ray and magnetic susceptibility data from F4 downhole logging)
672 and tephrochronological data (WDS-EMPA major element compositions and $^{40}\text{Ar}/^{39}\text{Ar}$ dating) consistently
673 indicate that new F4-F5 succession extends the previously established 190 kyr-long tephrostratigraphic and
674 palaeoenvironmental records from the F1-F3 succession, back to 430 ka. Specifically, major element
675 composition of the glass from eleven selected out of the ~130 macroscopically visible tephra layers that occur
676 in the F4-F5 record, as well as new geochemical data from two proximal pyroclastic units of the Vulsini and
677 Sabatini volcanic districts, enabled us to correlate them to known eruptions and/or tephra units, either already
678 previously recognised in the 0-190 ka interval of F1-F3 (Albano 7, Albano 5, Albano 3, Y-7, X-5, and Taurano
679 Ignimbrite) or identified in the 200-430 ka interval for the first time. These latter are: TF-62, correlated to the
680 Tufo Giallo di Sacrofano caldera-forming eruption, from Sabatini (288 ± 2 ka); TF-85, correlated to Villa
681 Senni caldera-forming eruption, Colli Albani (367.5 ± 1.6 ka); TF-117 and TF-118, correlated to the Pozzolane
682 Nere caldera-forming eruption and its precursor, Colli Albani (405 ± 2 ka, and 407 ± 4.2 ka, respectively); and
683 TF-126, correlated to Castel Broco Plinian eruption, Vulsini (419-490 ka). In particular, TF-126 has been here
684 $^{40}\text{Ar}/^{39}\text{Ar}$ dated at 424.3 ± 3.2 ka, thus providing a direct chronological constrain for the base of the core F4-
685 F5 and a first indirect, but much more precise, age for the poorly constrained Castel Broco Plinian eruption.

686 Through tephra synchronizations, supported by palaeoenvironmental proxy alignments, we combine the F1-
687 F3 and F4-F5 records in a composite F1-F3/F4-F5 tephra record. With its ~130 ash layers spanning the last
688 430 ka, the Fucino lacustrine succession is confirmed to be the most promising sedimentary archive for getting
689 a long, continuous and rich record of stratigraphically ordered tephra of the whole Mediterranean area. Future
690 developments of the ongoing investigations of the F4-F5 sedimentary cores are unavoidably intended to
691 expand the potential of the Fucino succession as a key, reference tephrochronological record, at the service of
692 a wide spectrum of the Quaternary sciences, including palaeoclimatology, palaeomagnetism, archaeology,
693 Quaternary geology, active tectonics and volcanology, on a geographic scale that extends from local to extra-
694 regional.

695

696 **Acknowledgements**

697 This article is a contribution of project “FUCino Tephrochronology Unites Quaternary REcords (FUTURE)”,
698 supported by the Italian Ministry of Education, University and Research (MIUR, grant PRIN No.
699 20177TKBXZ_003; G. Zanchetta, coordinator). An international consortium, including IGAG-CNR, IGG-
700 CNR, University of Pisa, INGV-Roma, LIAG-Hannover, University of Cologne, University of Rome La
701 Sapienza, University of Geneva, University of Nottingham, provided the funding for supporting the 2017
702 Fucino drilling campaign. We thank Antonello Provenzale for the additional financial support offered for
703 drilling. The $^{40}\text{Ar}/^{39}\text{Ar}$ age was supported by the CNRS INSU LEFE action to S. Nomade. The Fucino project

704 is co-funded by DFG (German Research Foundation) grant WA 2109/16. Two anonymous reviewers provided
705 thoughtful and constructive comments that improved the manuscript.

706
707

708 References

- 709 Amato, V., Aucelli, P.P.C., Cesarano, M., Filocamo, F., Leone, N., Petrosino, P., Roskopf, C.M., Valente, E., Casciello, E., Giralt, S.,
710 Jicha, B.R., 2018. Geomorphic response to late Quaternary tectonics in the axial portion of the Southern Apennines (Italy): A
711 case study from the Calore River valley. *Earth Surface Processes and Landforms* 43, 2463-2480.
- 712 Amato, V., Aucelli, P.P.C., Cesarano, M., Jicha, B., Lebreton, V., Orain, R., Pappone, G., Petrosino, P., Ermolli, E.R., 2014. Quaternary
713 evolution of the largest intermontane basin of the Molise Apennine (central-southern Italy). *Rendiconti Lincei* 25, 197-216.
- 714 Barberi, F., Buonasorte, G., Cioni, R., Fiordelisi, A., Foresi, L., Iaccarion, S., Laurenzi, M.A., Sbrana, A., Verenia, L., Villa, I.M.,
715 1994. Plio-Pleistocene geological evolution of the geothermal area of Tuscany and Latium. *Memorie Descrittive della Carta*
716 *Geologica d'Italia* 49, 77-134.
- 717 Bigazzi, G., Bonadonna, F., Cioni, R., Leone, G., Sbrana, A., Zanchetta, G., 1994. Nuovi dati geochimici, petrografici e geocronologici
718 su alcune cineriti Plio-Pleistoceniche del Lazio e della Toscana. *Memorie descrittive della Carta Geologica d'Italia* 49, 135-
719 150.
- 720 Blockley, S.P.E., Bourne, A.J., Brauer, A., Davies, S.M., Hardiman, M., Harding, P.R., Lane, C.S., MacLeod, A., Matthews, I.P., Pyne-
721 O'Donnell, S.D.F., Rasmussen, S.O., Wulf, S., Zanchetta, G., 2014. Tephrochronology and the extended intimate (integration
722 of ice-core, marine and terrestrial records) event stratigraphy 8–128 ka b2k. *Quaternary Science Reviews* 106, 88-100.
- 723 Bourne, A.J., Albert, P.G., Matthews, I.P., Trincardi, F., Wulf, S., Asioli, A., Blockley, S.P.E., Keller, J., Lowe, J.J., 2015.
724 Tephrochronology of core PRAD 1-2 from the Adriatic Sea: insights into Italian explosive volcanism for the period 200-80 ka.
725 *Quaternary Science Reviews* 116, 28-43.
- 726 Bourne, A.J., Lowe, J.J., Trincardi, F., Asioli, A., Blockley, S.P.E., Wulf, S., Matthews, I.P., Piva, A., Vigliotti, L., 2010. Distal tephra
727 record for the last ca 105,000 years from core PRAD 1-2 in the central Adriatic Sea implications for marine tephrostratigraphy.
728 *Quaternary Science Reviews* 29, 3079-3094.
- 729 Cavinato, G.P., Carusi, C., Dall'Asta, M., Miccadei, E., Piacentini, T., 2002. Sedimentary and tectonic evolution of Plio–Pleistocene
730 alluvial and lacustrine deposits of Fucino Basin (central Italy). *Sedimentary Geology* 148, 29-59.
- 731 Channell, J. E. T., 2006. Late Brunhes polarity excursions (Mono Lake, Laschamp, Iceland Basin and Pringle Falls) recorded at ODP
732 Site 919 (Irminger Basin): *Earth and Planetary Science Letters*, v. 244, no. 1, p. 378-393.
- 733 Channell, J. E. T., 2014. The Iceland Basin excursion: Age, duration, and excursion field geometry: *Geochemistry, Geophysics,*
734 *Geosystems*, v. 15, no. 12, p. 4920-4935.
- 735 Cheng H, Edwards RL, Sinha A, Spötl C, Yi L, Chen S, Kelly M, Kathayat G, Wang X, Li X, Kong X, Wang Y, Ning Y, Zhang H.
736 2016. The Asian monsoon over the past 640,000 years and ice age terminations. *Nature*. 2016 Jun 30;534(7609):640-6. doi:
737 10.1038/nature18591.
- 738 De Vivo, B., Rolandi, G., Gans, P.B., Calvert, A., Bohron, W.A., Spera, F.J., Belkin, H.E., 2001. New constraints on the pyroclastic
739 eruptive history of the Campanian volcanic Plain (Italy). *Mineralogy and Petrology* 73, 47-65.
- 740 Di Roberto, A., Smedile, A., Del Carlo, P., De Martini, P.M., Iorio, M., Petrelli, M., Pantosti, D., Pinzi, S., Todrani, A., 2018. Tephra
741 and cryptotephra in a ~60,000-year-old lacustrine sequence from the Fucino Basin: new insights into the major explosive
742 events in Italy. *Bulletin of Volcanology* 80, 20.
- 743 Follieri, M., Magri, D., Sadori, L., 1986. Late Pleistocene Zelkova extinction in Central Italy. *New Phytologist* 103, 269-273.
- 744 Follieri, M., Magri, D., Sadori, L., Villa, I., 1991. Palinologia e datazione radiometrica $^{40}\text{Ar}/^{39}\text{Ar}$ di un sondaggio nella piana del Fucino
745 (Abruzzo), Workshop 'Evoluzione dei bacini neogenici e loro rapporti con il magmatismo plioquaternario nell'area tosco-
746 laziale', Pisa, Italy, 12-13. Giugno, pp. 90-92.
- 747 Freda, C., Gaeta, M., Karner, D.B., Marra, F., Renne, P.R., Taddeucci, J., Scarlato, P., Christensen, J.N., Dallai, L., 2006. Eruptive
748 history and petrologic evolution of the Albano multiple maar (Alban Hills, Central Italy). *Bulletin of Volcanology* 68, 567-
749 591.
- 750 Galadini, F., Galli, P., 2000. Active Tectonics in the Central Apennines (Italy) – Input Data for Seismic Hazard Assessment. *Natural*
751 *Hazards* 22, 225-268.
- 752 Galadini, F., Messina, P., Giaccio, B., Sposato, A., 2003. Early uplift history of the Abruzzi Apennines (central Italy): available
753 geomorphological constraints. *Quaternary International* 101, 125-135.
- 754 Galli, P., Giaccio, B., Messina, P., Peronace, E., 2016. Three magnitude 7 earthquakes on a single fault in central Italy in 1400 years,
755 evidenced by new palaeoseismic results. *Terra Nova* 28, 146-154.
- 756 Galli, P., Giaccio, B., Messina, P., Peronace, E., Amato, V., Naso, G., Nomade, S., Pereira, A., Piscitelli, S., Bellanova, J., Billi, A.,
757 Blamart, D., Galderisi, A., Giocoli, A., Stabile, T., Thil, F., 2017. Middle to Late Pleistocene activity of the northern Matese
758 fault system (southern Apennines, Italy). *Tectonophysics* 699, 61-81.
- 759 Gatta, M., Giaccio, B., Marra, F., Rolfo, M.F., Jicha, B.R., 2017. Trace-element fingerprinting of the 69–36 ka Colli Albani eruptive
760 units: A preliminary dataset for archaeological and tephra studies in central-southern Italy. *Journal of Archaeological Science:*
761 *Reports* 16, 330-340.
- 762 Giaccio, B., Arienzo, I., Sottili, G., Castorina, F., Gaeta, M., Nomade, S., Galli, P., Messina, P., 2013a. Isotopic (Sr-Nd) and major
763 element fingerprinting of distal tephra: an application to the Middle-Late Pleistocene markers from the Colli Albani volcano,
764 central Italy. *Quaternary Science Reviews* 67, 190-206.
- 765 Giaccio, B., Castorina, F., Nomade, S., Scardia, G., Voltaggio, M., Sagnotti, L., 2013b. Revised Chronology of the Sulmona Lacustrine
766 Succession, Central Italy. *Journal of Quaternary Science* 28, 545-551.
- 767 Giaccio, B., Galli, P., Messina, P., Peronace, E., Scardia, G., Sottili, G., Sposato, A., Chiarini, E., Jicha, B., Silvestri, S., 2012a. Fault
768 and basin depocentre migration over the last 2 Ma in the L'Aquila 2009 earthquake region, central Italian Apennines.
769 *Quaternary Science Reviews* 56, 69-88.

770 Giaccio, B., Galli, P., Peronace, E., Arienzo I., Nomade, S., Cavinato, G.P., Mancini, M., Messina, P., Sottili, G., 2014. A 560-440 ka
771 tephra record from the Mercure Basin, Southern Italy: volcanological and tephrostratigraphic implications. *Journal of*
772 *Quaternary Science* 29, 232-248.

773 Giaccio, B., Hajdas, I., Isaia, R., Deino, A., Nomade, S., 2017a. High-precision ¹⁴C and ⁴⁰Ar/³⁹Ar dating of the Campanian Ignimbrite
774 (Y-5) reconciles the time-scales of climatic-cultural processes at 40 ka. *Scientific Reports* 7, 45940.

775 Giaccio, B., Marra, F., Hajdas, I., Karner, D.B., Renne, P.R., Sposato, A., 2009. ⁴⁰Ar/³⁹Ar and ¹⁴C geochronology of the Albano
776 maar deposits: Implications for defining the age and eruptive style of the most recent explosive activity at Colli Albani Volcanic
777 District, Central Italy. *Journal of Volcanology and Geothermal Research* 185, 203-213.

778 Giaccio, B., Niespolo, E.M., Pereira, A., Nomade, S., Renne, P.R., Albert, P.G., Arienzo, I., Regattieri, E., Wagner, B., Zanchetta, G.,
779 Gaeta, M., Galli, P., Mannella, G., Peronace, E., Sottili, G., Florindo, F., Leicher, N., Marra, F., Tomlinson, E.L., 2017. First
780 integrated tephrochronological record for the last ~190 kyr from the Fucino Quaternary lacustrine succession, central Italy.
781 *Quaternary Science Reviews* 158, 211-234.

782 Giaccio, B., Nomade, S., Wulf, S., Isaia, R., Sottili, G., Cavuoto, G., Galli, P., Messina, P., Sposato, A., Sulpizio, R., Zanchetta, G.,
783 2012b. The late MIS 5 Mediterranean tephra markers: a reappraisal from peninsular Italy terrestrial records. *Quaternary Science*
784 *Reviews* 56, 31-45.

785 Giaccio, B., Regattieri, E., Zanchetta, G., Nomade, S., Renne, P.R., Sprain, C.J., Drysdale, R.N., Tzedakis, P.C., Messina, P., Scardia,
786 G., Sposato, A., Bassinot, F., 2015a. Duration and dynamics of the best orbital analogue to the present interglacial. *Geology*
787 43, 603-606.

788 Giaccio, B., Regattieri, E., Zanchetta, G., Wagner, B., Galli, P., Mannella, G., Niespolo, E., Peronace, E., Renne, P.R., Nomade, S.,
789 Cavinato, G.P., Messina, P., Sposato, A., Boschi, C., Florindo, F., Marra, F., Sadori, L., 2015b. A key continental archive for
790 the last 2 Ma of climatic history of the central Mediterranean region: A pilot drilling in the Fucino Basin, central Italy. *Scientific*
791 *Drilling* 20, 13-19.

792 Giaccio, B., Sposato, A., Gaeta, M., Marra, F., Palladino, D.M., Taddeucci, J., Barbieri, M., Messina, P., Rolfo, M.F., 2007. Mid-distal
793 occurrences of the Albano Maar pyroclastic deposits and their relevance for reassessing the eruptive scenarios of the most
794 recent activity at the Colli Albani Volcanic District, Central Italy. *Quaternary International* 171-172, 160-178.

795 Giordano, G., De Benedetti, A.A., Diana, A., Diano, G., Gaudio, F., Marasco, F., Miceli, M., Mollo, S., Cas, R.A.F., Funicello, R.,
796 2006. The Colli Albani mafic caldera (Roma, Italy): Stratigraphy, structure and petrology. *Journal of Volcanology and*
797 *Geothermal Research* 155, 49-80.

798 Giraudi, C., Giaccio, B., 2015. Middle Pleistocene glaciations in the Apennines, Italy: new chronological data and preservation of the
799 glacial record. *Geological Society, London, Special Publications* 433, 161-178.

800 Govin, A., Capron, E., Tzedakis, P.C., Verheyden, S., Ghaleb, B., Hillaire-Marcel, C., St-Onge, G., Stoner, J.S., Bassinot, F., Bazin,
801 L., Blunier, T., Combourieu-Nebout, N., El Ouahabi, A., Genty, D., Gersonde, R., Jimenez-Amat, P., Landais, A., Martrat, B.,
802 Masson-Delmotte, V., Parrenin, F., Seidenkrantz, M.S., Veres, D., Waelbroeck, C., Zahn, R., 2015. Sequence of events from
803 the onset to the demise of the Last Interglacial: Evaluating strengths and limitations of chronologies used in climatic archives.
804 *Quaternary Science Reviews* 129, 1-36.

805 Gouhier, T., Grinsted, A., Simko, V., 2018. biwavelet: Conduct univariate and bivariate wavelet analyses. R Package Version 02017.

806 Insinga, D.D., Tamburrino, S., Lirer, F., Vezzoli, L., Barra, M., De Lange, G.J., Tiepolo, M., Vallefucio, M., Mazzola, S., Sprovieri,
807 M., 2014. Tephrochronology of the astronomically-tuned KC01B deep-sea core, Ionian Sea: insights into the explosive activity
808 of the Central Mediterranean area during the last 200 ka. *Quaternary Science Reviews* 85, 63-84.

809 Karner, D.B., Juvigne, E., Brancaccio, L., Cinque, A., Russo Ermolli, E., Santangelo, N., Bernasconi, S., Lirer, L., 1999. A potential
810 early middle Pleistocene tephrostratotype for the Mediterranean Basin: the Vallo di Diano, Campania, Italy. *Global and*
811 *Planetary Change* 21, 1-15.

812 Karner, D.B., Marra, F., Renne, P.R., 2001. The history of the Monti Sabatini and Alban Hills volcanoes: groundwork for assessing
813 volcanic-tectonic hazards for Rome. *Journal of Volcanology and Geothermal Research* 107, 185-219.

814 Kousis, I., Koutsodendris, A., Peyron, O., Leicher, N., Francke, A., Wagner, B., Giaccio, B., Knipping, M., Pross, J., 2018. Centennial-
815 scale vegetation dynamics and climate variability in SE Europe during Marine Isotope Stage 11 based on a pollen record from
816 Lake Ohrid. *Quaternary Science Reviews* 190, 20-38.

817 Lane, C.S., Lowe, D.J., Blockley, S.P.E., Suzuki, T., Smith, V.C., 2017. Advancing tephrochronology as a global dating tool:
818 Applications in volcanology, archaeology, and palaeoclimatic research. *Quaternary Geochronology* 40, 1-7.

819 Laurenzi, M.A., Villa, I., 1987. ⁴⁰Ar/³⁹Ar chronostratigraphy of Vico ignimbrites. *Periodico di Mineralogia* 56, 285-293.

820 Le Bas, M.J.L., Maitre, R.W.L., Streckeisen, A., Zanettin, B., 1986. A Chemical Classification of Volcanic Rocks Based on the Total
821 Alkali-Silica Diagram. *Journal of Petrology* 27, 745-750.

822 Lee, J.Y., Marti, K., Severinghaus, J.P., Kawamura, K., Yoo, H.S., Lee, J.B., Kim, J.S., 2006. A redetermination of the isotopic
823 abundances of atmospheric Ar. *Geochimica Et Cosmochimica Acta* 70, 4507-4512.

824 Leicher, N., Zanchetta, G., Sulpizio, R., Giaccio, B., Wagner, B., Nomade, S., Francke, A., Del Carlo, P., 2016. First tephrostratigraphic
825 results of the DEEP site record from Lake Ohrid (Macedonia and Albania). *Biogeosciences* 13, 2151-2178.

826 Lisiecki, L.E., Raymo, M.E., 2005. A Pliocene-Pleistocene stack of 57 globally distributed benthic $\delta^{18}O$ records. *palaeoceanography*
827 20, PA1003.

828 Litt, T., Anselmetti, F.S., 2014. Lake Van deep drilling project PALAEOVAN. *Quaternary Science Reviews* 104, 1-7.

829 Lowe, J.J., Ramsey, C.B., Housley, R.A., Lane, C.S., Tomlinson, E.L., 2015. The RESET project: constructing a European tephra
830 lattice for refined synchronisation of environmental and archaeological events during the last c. 100 ka. *Quaternary Science*
831 *Reviews* 118, 1-17.

832 Mannella, G., Giaccio, B., Zanchetta, G., Regattieri, E., Niespolo, E.M., Pereira, A., Renne, P.R., Nomade, S., Leicher, N., Perchiazzi,
833 N., Wagner, B., 2019. Palaeoenvironmental and palaeohydrological variability of mountain areas in the central Mediterranean
834 region: A 190 ka-long chronicle from the independently dated Fucino palaeolake record (central Italy). *Quaternary Science*
835 *Reviews* 210, 190-210.

- 836 Marra, F., Gaeta, M., Giaccio, B., Jicha, B.R., Palladino, D.M., Polcari, M., Sottili, G., Taddeucci, J., Florindo, F., Stramondo, S.,
837 2016. Assessing the volcanic hazard for Rome: $^{40}\text{Ar}/^{39}\text{Ar}$ and In-SAR constraints on the most recent eruptive activity and
838 present-day uplift at Colli Albani Volcanic District. *Geophysical Research Letters* 43, 6898-6906.
- 839 Marra, F., Karner, D.B., Freda, C., Gaeta, M., Renne, P., 2009. Large mafic eruptions at Alban Hills Volcanic District (Central Italy):
840 Chronostratigraphy, petrography and eruptive behavior. *Journal of Volcanology and Geothermal Research* 179, 217-232.
- 841 Marra, F., Rohling, E.J., Florindo, F., Jicha, B., Nomade, S., Pereira, A., Renne, P.R., 2016. Independent $^{40}\text{Ar}/^{39}\text{Ar}$ and ^{14}C age
842 constraints on the last five glacial terminations from the aggradational successions of the Tiber River, Rome (Italy). *Earth
843 Planet Sci Lett.*, 449, 105-117.
- 844 Marra, F., Sottili, G., Gaeta, M., Giaccio, B., Jicha, B., Masotta, M., Palladino, D.M., Deocampo, D.M., 2014. Major explosive activity
845 in the Monti Sabatini Volcanic District (central Italy) over the 800-390 ka interval: geochronological-geochemical overview
846 and tephrostratigraphic implications. *Quaternary Science Reviews* 94, 74-101.
- 847 Marra, F., Bahain, J.-J., Jicha, B., Nomade, S., Palladino, D.M., Pereira, A., Tolomei, C., Voinchet, P., Anzidei, M., Aureli, D., Ceruleo,
848 P., Falguères, C., Florindo, F., Gatta, M., Ghaleb, B., La Rosa, M., Peretto, C., Petronio, C., Rocca, R., Rolfo, M.F., Salari, L.,
849 Smedile, A., Tombret, O., 2019. Reconstruction of the MIS 5.5, 5.3 and 5.1 coastal terraces in Latium (central Italy): a re-
850 evaluation of the sea-level history in the Mediterranean Sea during the Last Interglacial. *Quaternary International* 525, 54-
851 77. DOI:10.1016/j.quaint.2019.09.001.
- 852 Martrat, B., Grimalt, J.O., Shackleton, N.J., de Abreu, L., Hutterli, M.A., Stocker, T.F., 2007. Four climate cycles of recurring deep
853 and surface water destabilizations on the Iberian margin. *Science* 317, 502-507.
- 854 Munno, R., Petrosino, P., 2007. The late Quaternary tephrostratigraphical record of the San Gregorio Magno basin (southern Italy).
855 *Journal of Quaternary Science* 22, 247-266.
- 856 Narcisi, B., 1994. Caratteristiche e possibile provenienza di due livelli piroclastici nei sedimenti del Pleistocene superiore della piana
857 del Fucino (Italia Centrale). *Rendiconti Lincei* 5, 115.
- 858 Niespolo, E.M., Rutte, D., Deino, A.L., Renne, P.R., 2017. Intercalibration and age of the Alder Creek sanidine $^{40}\text{Ar}/^{39}\text{Ar}$ standard.
859 *Quaternary Geochronology* 39, 205-213.
- 860 Palladino, D.M., Simei, S., Sottili, G., Trigila, R., 2010. Integrated approach for the reconstruction of stratigraphy and geology of
861 Quaternary volcanic terrains: An application to the Vulsini Volcanoes (Central Italy). *Geological Society of America Special
862 Papers* 464, 63-84.
- 863 Paterne, M., Guichard, F., Duplessy, J.C., Siani, G., Sulpizio, R., Labeyrie, J., 2008. A 90,000–200,000 yrs marine tephra record of
864 Italian volcanic activity in the Central Mediterranean Sea. *Journal of Volcanology and Geothermal Research* 177, 187-196.
- 865 Peccerillo, A., 2017. Cenozoic volcanism in the Tyrrhenian Sea region, in: IAVCEI (Ed.), *Advances in Volcanology*, 2 ed. Springer,
866 p. 399.
- 867 Pereira, A., Nomade, S., Falguères, C., Bahain, J.-J., Tombret, O., Garcia, T., Voinchet, P., Bulgarelli, G.-M., Anzidei, A.-P., 2017.
868 $^{40}\text{Ar}/^{39}\text{Ar}$ and ESR/U-series data for the La Polledrara di Cecanibbio archaeological site (Lazio, Italy). *Journal of
869 Archaeological Science: Reports* 15, 20-29.
- 870 Pereira, A., Nomade, S., Moncel, M.H., Voinchet, P., Bahain, J.J., Biddittu, I., Falgueres, C., Giaccio, B., Manzi, G., Parenti, F.,
871 Scardia, G., Scao, V., Sottili, G., Vietti, A., 2018. Integrated geochronology of Acheulian sites from the southern Latium
872 (central Italy): Insights on human-environment interaction and the technological innovations during the MIS 11-MIS 10 period.
873 *Quaternary Science Reviews* 187, 112-129.
- 874 Perini, G., Francalanci, L., Davidson, J.P., Conticelli, S., 2004. Evolution and genesis of magmas from Vico Volcano, Central Italy:
875 multiple differentiation pathways and variable parental magmas. *Journal of Petrology* 45, 139-182.
- 876 Petrosino, P., Ermolli, E.R., Donato, P., Jicha, B., Robustelli, G., Sardella, R., 2014a. Using Tephrochronology and palynology to date
877 the MIS 13 lacustrine sediments of the Mercure Basin (Southern Apennines – Italy). *Italian Journal of Geosciences* 133, 169-
878 186.
- 879 Petrosino, P., Jicha, B.R., Mazzeo, F.C., Russo Ermolli, E., 2014b. A high resolution tephrochronological record of MIS 14–12 in the
880 Southern Apennines (Acerno Basin, Italy). *Journal of Volcanology and Geothermal Research* 274, 34-50.
- 881 Petrosino, P., Morabito, S., Jicha, B.R., Milia, A., Sprovieri, M., Tamburrino, S., 2016. Multidisciplinary tephrochronological
882 correlation of marker events in the eastern Tyrrhenian Sea between 48 and 105ka. *Journal of Volcanology and Geothermal
883 Research* 315, 79-99.
- 884 Railsback, L.B., Gibbard, P.L., Head, M.J., Voarintsoa, N.R.G., Toucanne, S., 2015. An optimized scheme of lettered marine isotope
885 substages for the last 1.0 million years, and the climatostratigraphic nature of isotope stages and substages. *Quaternary Science
886 Reviews* 111, 94-106.
- 887 R Core Team, 2017. *R: A Language and Environment for Statistical Computing*.
- 888 Regattieri, E., Giaccio, B., Galli, P., Nomade, S., Peronace, E., Messina, P., Sposato, A., Boschi, C., Gemelli, M., 2016. A multi-proxy
889 record of MIS 11–12 deglaciation and glacial MIS 12 instability from the Sulmona basin (central Italy). *Quaternary Science
890 Reviews* 132, 129-145.
- 891 Regattieri, E., Giaccio, B., Mannella, G., Zanchetta, G., Nomade, S., Tognarelli, A., Perchiazzi, N., Vogel, H., Boschi, C., Drysdale,
892 R.N., Wagner, B., Gemelli, M., Tzedakis, P., 2019. Frequency and dynamics of millennial-scale variability during Marine
893 Isotope Stage 19: Insights from the Sulmona Basin (central Italy). *Quaternary Science Reviews* 214, 28-43.
- 894 Regattieri, E., Giaccio, B., Zanchetta, G., Drysdale, R.N., Galli, P., Nomade, S., Peronace, E., Wulf, S., 2015. Hydrological variability
895 over the Apennines during the Early Last Glacial precession minimum, as revealed by a stable isotope record from Sulmona
896 basin, Central Italy. *Journal of Quaternary Science* 30, 19-31.
- 897 Renne, P.R., Balco, G., Ludwig, K.R., Mundil, R., Min, K., 2011. Response to the comment by WH Schwarz et al. on “Joint
898 determination of 40 K decay constants and $^{40}\text{Ar}/^{40}\text{K}$ for the Fish Canyon sanidine standard, and improved accuracy for $^{40}\text{Ar}/^{39}\text{Ar}$
899 geochronology” by PR Renne et al.(2010). *Geochimica et Cosmochimica Acta* 75, 5097-5100.
- 900 Rodrigues, T., Alonso-Garcia, M., Hodell, D.A., Rufino, M., Naughton, F., Grimalt, J.O., Voelker, A.H.L., Abrantes, F., 2017. A 1-
901 Ma record of sea surface temperature and extreme cooling events in the North Atlantic: A perspective from the Iberian Margin.
902 *Quaternary Science Reviews* 172, 118-130.

- 903 Rodrigues, T., Voelker, A.H.L., Grimalt, J.O., Abrantes, F., Naughton, F., 2011. Iberian Margin sea surface temperature during MIS
904 15 to 9 (580–300 ka): Glacial suborbital variability versus interglacial stability. *palaeoceanography and palaeoclimatology* 26,
905 PA1204.
- 906 Russo Ermolli, E. R., Di Donato, V., Martín-Fernández, J. A., Orain, R., Lebreton, V., & Piovesan, G., 2015. Vegetation patterns in
907 the Southern Apennines (Italy) during MIS 13: deciphering pollen variability along a NW-SE transect. *Review of Palaeobotany*
908 and *Palynology*, 218, 167-183
- 909 Sbrana, A., Toccaceli, R.M., 2011. Geological Map of “Isola di Ischia”, 1: 10000 Scale, Foglio 464. Regione Campania-Assessorato
910 difesa del suolo, Firenze.
- 911 Scholz, D., Hoffmann, D.L., 2011. StalAge – An algorithm designed for construction of speleothem age models. *Quaternary*
912 *Geochronology* 6, 369-382.
- 913 Singer, B. S., Guillou, H., Jicha, B. R., Zanella, E., and Camps, P., 2014, Refining the Quaternary Geomagnetic Instability Time Scale
914 (GITS): Lava flow recordings of the Blake and Post-Blake excursions: *Quaternary Geochronology*, v. 21, p. 16-28.
- 915 Smith, V.C., Isaia, R., Pearce, N.J.G., 2011. Tephrostratigraphy and glass compositions of post-15 kyr Campi Flegrei eruptions:
916 implications for eruption history and chronostratigraphic markers. *Quaternary Science Reviews* 30, 3638-3660.
- 917 Sottili, G., Palladino, D.M., Marra, F., Jicha, B., Karner, D.B., Renne, P., 2010. Geochronology of the most recent activity in the
918 Sabatini Volcanic District, Roman Province, central Italy. *Journal of Volcanology and Geothermal Research* 196, 20-30.
- 919 Sottili, G., Palladino, D.M., Zanon, V., 2004. Plinian activity during the early eruptive history of the Sabatini volcanic district, central
920 Italy. *Journal of Volcanology and Geothermal Research* 135, 361-379.
- 921 Sulpizio, R., Zanchetta, G., D’Orazio, M., Vogel, H., Wagner, B., 2010. Tephrostratigraphy and tephrochronology of Lakes Ohrid and
922 Prespa, Balkans. *Biogeosciences* 7, 3273-3288.
- 923 Tamburrino, S., Insinga, D.D., Sprovieri, M., Petrosino, P., Tiepolo, M., 2012. Major and trace element characterization of tephra
924 layers offshore Pantelleria Island: insights into the last 200 ka of volcanic activity and contribution to the Mediterranean
925 tephrochronology. *Journal of Quaternary Science* 27, 129-140.
- 926 Tauxe, L., 1993. Sedimentary records of relative paleointensity of the geomagnetic field: Theory and practice. *Reviews of*
927 *Geophysics*, 31(3), 319-354.
- 928 Tomlinson, E.L., Albert, P.G., Wulf, S., Brown, R.J., Smith, V.C., Keller, J., Orsi, G., Bourne, A.J., Menzies, M.A., 2014. Age and
929 geochemistry of tephra layers from Ischia, Italy: constraints from proximal-distal correlations with Lago Grande di Monticchio.
930 *Journal of Volcanology and Geothermal Research* 287, 22-39.
- 931 Vakhrameeva, P., Koutsodendris, A., Wulf, S., Fletcher, W.J., Appelt, O., Knipping, M., Gertisser, R., Trieloff, M., Pross, J., 2018.
932 The cryptotephra record of the Marine Isotope Stage 12 to 10 interval (460–335 ka) at Tenaghi Philippon, Greece: Exploring
933 chronological markers for the Middle Pleistocene of the Mediterranean region. *Quaternary Science Reviews* 200, 313-333.
- 934 Vakhrameeva, P., Wulf, S., Koutsodendris, A., Tjallingii, R., Fletcher, W.J., Appelt, O., Ludwig, T., Knipping, M., Trieloff, M., Pross,
935 J., 2019. Eastern Mediterranean volcanism during marine isotope stages 9 to 7e (335–235 ka): Insights based on cryptotephra
936 layers at Tenaghi Philippon, Greece. *Journal of Volcanology and Geothermal Research* 380, 31-47.
- 937 Vazquez, J. A., and Lidzbarski, M. I., 2012, High-resolution tephrochronology of the Wilson Creek Formation (Mono Lake, California)
938 and Laschamp event using 238U-230Th SIMS dating of accessory mineral rims: *Earth and Planetary Science Letters*, v. 357-
939 358, p. 54-67.
- 940 Wastegård, S., Veres, D., Kliem, P., Hahn, A., Ohlendorf, C., Zolitschka, B., Team, T.P.S., 2013. Towards a late Quaternary
941 tephrochronological framework for the southernmost part of South America—the Laguna Potrok Aike tephra record. *Quaternary*
942 *Science Reviews* 71, 81-90.
- 943 Wulf, S., Keller, J., Paterne, M., Mingram, J., Lauterbach, S., Opitz, S., Sottili, G., Giaccio, B., Albert, P.G., Satow, C., Tomlinson,
944 E.L., Viccaro, M., Brauer, A., 2012. The 100–133 ka record of Italian explosive volcanism and revised tephrochronology of
945 Lago Grande di Monticchio. *Quaternary Science Reviews* 58, 104-123.
- 946 Wulf, S., Kraml, M., Brauer, A., Keller, J., Negendank, J.F.W., 2004. Tephrochronology of the 100ka lacustrine sediment record of
947 Lago Grande di Monticchio (Southern Italy). *Quaternary International* 122, 7-30.
- 948 Zanchetta, G., Giaccio, B., Bini, M., Sarti, L., 2018. Tephrostratigraphy of Grotta del Cavallo, Southern Italy: Insights on the
949 chronology of Middle to Upper Palaeolithic transition in the Mediterranean. *Quaternary Science Reviews* 182, 65-77.
- 950 Zanchetta, G., Sulpizio, R., Giaccio, B., Siani, G., Paterne, M., Wulf, S., D’Orazio, M., 2008. The Y-3 tephra: A Last Glacial
951 stratigraphic marker for the Central Mediterranean Basin. *Journal of Volcanology and Geothermal Research* 177, 145-154.

952

953

954 **Figure and Table captions**

955

956 **Table 1.** Analysed tephra layers from core F4-F5.

957

958 **Figure 1.** Reference map of the Fucino Basin. (a) Location of Fucino Basin with respect to the main Quaternary
959 Italian volcanic centres. (b) Shaded relief map showing the location of the GL, TS, SP, F1-F3 (Giaccio et al.,
960 2015b; 2017a), F4-F5 (Mannella et al., 2019, this study), FUC-S5-6 (Di Roberto et al., 2018) boreholes in the
961 Fucino Basin. See legend in inset for the meaning of symbols. (c) Seismic Line 1 (see trace in panel b) showing
962 the internal architecture of the Plio-Quaternary continental deposits of the Fucino Basin along a W-E oriented
963 profile (Cavinato et al., 2002). The projected location of various boreholes on Line 1 is also shown. Seismic
964 facies interpretation of the sedimentary infill is according to Cavinato et al. (2002).

965

966

967

968

969

Figure 2. Example of correlation between the overlapped F4 and F5 core sections and of the selection of the intervals used for building the composite F4-F5 record. Note that the gaps in-between two consecutive individual core sections of F4 borehole are documented in F5 borehole, and vice versa.

970

971

972

973

974

975

976

977

978

979

980

981

982

983

984

Figure 3. Tephrostratigraphy, selected proxy data and general chronological framework for the newly F4-F5 and the previously investigated F1-F3 (Giaccio et al., 2017; Mannella et al., 2019). **(a)** Magnetic susceptibility from Fucino F4 downhole logging (black) and its logarithmic representation (green) to show similarity to gamma ray and Ca data. **(b)** Gamma ray from Fucino F4 downhole logging. **(c)** Selected tephra from core F4-F5 investigated in this study. **(d)** Inclination data after the 16 mT AF step with tentative position of the Laschamp (LE) Blake and Iceland Basin (IBE) geomagnetic excursions. **(e)** Complete tephra record and Ca counts from XRF scanning in core F4-F5. Five stratigraphic intervals with relatively high Ca counts are highlighted in yellow and correlated to the warm Marine Isotope Stage (MIS) 1 to 11 (the threshold is at 22700 cps, see text for explanation). **(f)** Complete tephra record and Ca counts from XRF scanning in core F1-F3 (Giaccio et al., 2017; Mannella et al., 2019). **(g)** Combined tephrochronology of F1-F3 and F4-F5 core. **(h)** LR04 stack of marine benthic oxygen isotope records (Lisiecki and Raymo, 2005). Data source: $^{40}\text{Ar}/^{39}\text{Ar}$, ^{14}C , astrochronological, modelled ages and correlation of tephra of the last 190 kyr: Giaccio et al. (2017) and Mannella et al. (2019) and reference therein. The boundaries of the marine isotope stages (MIS) are according to Railsback et al. (2015).

985

986

987

988

989

990

991

992

Figure 4. Representative major element compositions for the analysed F4-F5 tephra layers. **(a)** Total alkali versus silica classification diagram (Le Bas et al., 1986) of the F4-F5 tephra distinguished in two compositional groups (CG1 and CG2). **(b)** CaO/FeO vs Cl discriminating diagram of the volcanic sources of the Italian potassic trachyte-phonolite and tephriphonolite tephra (modified from Giaccio et al., 2017) for the F4-F5 tephra. The CaO/FeO vs Cl diagram has been updated with the following data: Roccamonfina: Amato et al. (2014) and Galli et al. (2017); Vulcini, Vico Period I (P-I) and Period II (P-II) and Sabatini: this study and Author's unpublished data. For other references, the readers are referred to Giaccio et al. (2017).

993

994

995

996

Figure 5. Age probability density spectra diagram (left) and inverse isochrone (right) of tephra TF-126 (sampling code; F5-58 64-66). Blue and white bars/ indicate the individual ages included and discarded as weighted mean age, respectively.

997

998

999

1000

1001

1002

1003

1004

1005

Figure 6. Total alkali versus silica classification diagram after Le Bas et al. (1986) and representative bi-plots for the tephra F5-8 77-92 **(a)**, F5-8 148-155 **(b)** and F8-12 89-91 **(c)** from the F4-F5 record compared with their equivalents in core F1-F3. Data source: glass-WDS of Fucino TF-4, TF-5 and TF-8: Giaccio et al. (2017); $^{40}\text{Ar}/^{39}\text{Ar}$ age of Fucino TF-5: weighted mean of dating from (Freda et al., 2006; Giaccio et al., 2009; Giaccio et al., 2017), and Mannella et al. (2019); **glass composition of Albano 7 Colli Albani: Giaccio et al. (2007);** $^{40}\text{Ar}/^{39}\text{Ar}$ age of Albano 7 and Albano 3: weighted mean of dating from Freda et al. (2006) and Giaccio et al. (2007). $^{40}\text{Ar}/^{39}\text{Ar}$ ages are recalculated relative to an age of 1.1891 Ma for the Alder Creek sanidine monitor standard (Niespolo et al., 2017), with the uncertainty expressed at 2σ .

1006

1007

1008

1009

1010

1011

1012

1013

1014

1015

1016

1017

Figure 7. Total alkali versus silica classification diagram Le Bas et al. (1986) and representative bi-plots for the tephra F5-8 148-149 **(a)**, F5-15 90-91 **(b)**, F5-20 89-91 **(c)** from core F4-F5 compared with their equivalents in core F1-F3 and with some selected proximal or distal counterparts. For comparison, in panel **(b)** also the composition of X-6 layer (grey text), not correlated with F5-15 90-91, is showed. Data source: glass-WDS and $^{40}\text{Ar}/^{39}\text{Ar}$ age of Fucino TF-7: Giaccio et al. (2017); glass-WDS and $^{40}\text{Ar}/^{39}\text{Ar}$ age of Monte Epomeo Green Tuff: Tomlinson et al. (2014) and Sbrana and Toccaceli (2011), respectively; glass-WDS of PRAD-1870: Bourne et al. (2010); glass-WDS TF-12 and TF-13 Giaccio et al. (2017); glass-WDS and $^{40}\text{Ar}/^{39}\text{Ar}$ age of Sulmona POP3 and POP4 tephra layers: Giaccio et al. (2012b) and Regattieri et al. (2015), respectively; glass-EDS glass-WDS and $^{40}\text{Ar}/^{39}\text{Ar}$ age of TF-17: Giaccio et al. (2017); glass-EDS and $^{40}\text{Ar}/^{39}\text{Ar}$ age of CET1-18: Petrosino et al. (2016); glass-EDS and $^{40}\text{Ar}/^{39}\text{Ar}$ age of the proximal Taurano Ignimbrite: Amato et al. (2018) and De Vivo et al. (2001), respectively; glass-EDS and $^{40}\text{Ar}/^{39}\text{Ar}$ age of S11 PAUP: Amato et al. (2018). The tephra age reported on top of each figure panel is the weighted mean of the $^{40}\text{Ar}/^{39}\text{Ar}$ ages indicated in the

1018 respective panel. $^{40}\text{Ar}/^{39}\text{Ar}$ ages are recalculated relatively to an age of 1.1891 Ma for the Alder Creek sanidine
1019 monitor standard (Niespolo et al., 2017), with the uncertainty expressed at 2σ .

1020

1021 **Figure 8.** Total alkali versus silica classification diagram after Le Bas et al. (1986) and representative bi-plots
1022 for the tephra TF-85 (a), TF-117 (b), and TF-118 (c) from the F4-F5 record compared with their proximal or
1023 distal counterparts. Data source: glass-WDS and $^{40}\text{Ar}/^{39}\text{Ar}$ age of Villa Senni proximal units: (Marra et al.,
1024 2009, 2019); glass-WDS and $^{40}\text{Ar}/^{39}\text{Ar}$ age of Villa Senni distal (PAG-t4): (Giaccio et al., 2012a); glass-WDS
1025 and $^{40}\text{Ar}/^{39}\text{Ar}$ age Pozzolane Nere fallout: (glass-WDS): (Marra et al., 2009); glass-WDS and $^{40}\text{Ar}/^{39}\text{Ar}$ age
1026 Fontana Ranuccio 2 (glass-WDS): (Pereira et al., 2018). The tephra age reported on top of each figure panel is
1027 the weighted mean of the $^{40}\text{Ar}/^{39}\text{Ar}$ ages indicated in the respective panel. $^{40}\text{Ar}/^{39}\text{Ar}$ ages are recalculated
1028 relatively to an age of 1.1891 Ma for the Alder Creek sanidine monitor standard (Niespolo et al., 2017), with
1029 the uncertainty expressed at 2σ .

1030

1031 **Figure 9.** Total alkali versus silica classification diagram after Le Bas et al. (1986) and representative bi-plots
1032 for the tephra TF-62 (a) and TF-126 (b) of the F4-F5 succession compared with their proximal counterparts.
1033 TF-126 is also compared with some geochronologically compatible but geochemically different tephra R99-
1034 30C (Tiber River successions), OH-DP 1733 (Lake Ohrid) and MOL 13 (Bojano Basin). Data source: glass-
1035 WDS of Tufo Giallo di Sacrofano and Castel Broco: this study; $^{40}\text{Ar}/^{39}\text{Ar}$ age of Tufo Giallo di Sacrofano:
1036 Sottili et al. (2010); glass-WDS and $^{40}\text{Ar}/^{39}\text{Ar}$ age of R94-30C: this study and Marra et al. (2016) respectively;
1037 glass-WDS of OH-DP 1733: Leicher et al. (in review); glass-WDS of MOL 13: Amato et al. (2014). The tephra
1038 age reported on top of each figure panel is the weighted mean of the $^{40}\text{Ar}/^{39}\text{Ar}$ ages indicated in the respective
1039 panel. $^{40}\text{Ar}/^{39}\text{Ar}$ ages are recalculated relatively to an age of 1.1891 Ma for the Alder Creek sanidine monitor
1040 standard (Niespolo et al., 2017), with the uncertainty expressed at 2σ .

1041

1042 **Figure 10.** Detailed proxy and tephra correlation of the F1-F3 record with the corresponding interval in core
1043 F4-F5. The two tephra records are merged for a composite F1-F3/F4-F5 tephra record. Note that tephra found
1044 only in F1-F3 or F4-F5 are transferred from one to the other via climatostratigraphic positions.

1045

1046 **Figure 11.** Composite F1-F3/F4-F5 tephra record. References: ^a Mannella et al. (2019 and references therein);
1047 ^b Petrosino et al. (2016) ^c Amato et al. (2018); ^d De Vivo et al.. (2001); ^e Sottili et al. (2010); ^f Marra et al.
1048 (2009); ^g Marra et al. (2019); ^h Giaccio et al. (2012); ⁱ Pereira et al. (2018); ^j This study. $^{40}\text{Ar}/^{39}\text{Ar}$ ages are
1049 recalculated relatively to an age of 1.1891 Ma for the Alder Creek sanidine monitor standard (Niespolo et al.,
1050 2017), with the uncertainty expressed at 2σ .

1051

1052 **Figure 12.** Preliminary age model for the composite F1-F3/F4-F5 tephra and F4-F5 Ca and palaeomagnetic
1053 records. The Fucino calcium record is compared with the sea surface temperature (SST) record from the SW
1054 Iberian Margin core MD01-2444/43 (dark red, Martrat et al., 2007) and core U1385 (red Rodrigues et al.,
1055 2017). The boundaries of the marine isotope stages (MIS) Iberian Margin record and are projected in the
1056 Fucino record along the intercept points of the yellow/blue bars with the dashed green line, which is the linear
1057 interpolation between the mid-point of the tephra ages reported in Figure 9. The ages of Fucino tephras (dashed
1058 pink lines) are in turn projected in the time-scale of the Iberian Margin SST records, that are based on their
1059 own age models (Martrat et al., 2007; Rodrigues et al., 2011). The interceptions of the orange bars with the
1060 dashed green line also provide an age estimation for the Laschamp, Blake and Iceland Basin geomagnetic
1061 excursions, as inferred from the preliminary palaeomagnetic data.

1062

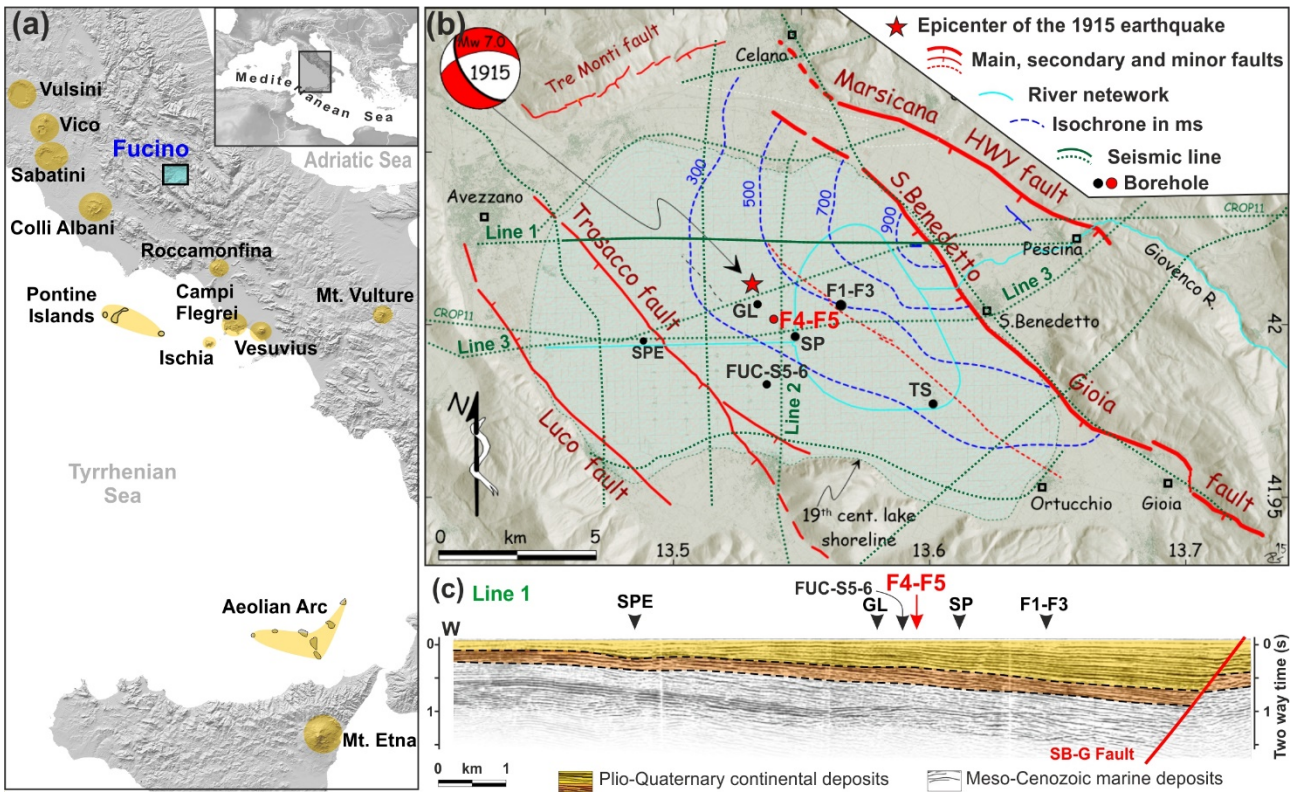


Figure 1. Reference map of the Fucino Basin. (a) Location of Fucino Basin with respect to the main Quaternary Italian volcanic centres. (b) Shaded relief map showing the location of the GL, TS, SP, F1-F3 (Giaccio et al., 2015b; 2017a), F4-F5 (Mannella et al., 2019, this study), FUC-S5-6 (Di Roberto et al., 2018) boreholes in the Fucino Basin. See legend in inset for the meaning of symbols. (c) Seismic Line 1 (see trace in panel b) showing the internal architecture of the Plio-Quaternary continental deposits of the Fucino Basin along a W-E oriented profile (Cavinato et al., 2002). The projected location of various boreholes on Line 1 is also shown. Seismic facies interpretation of the sedimentary infill is according to Cavinato et al. (2002).

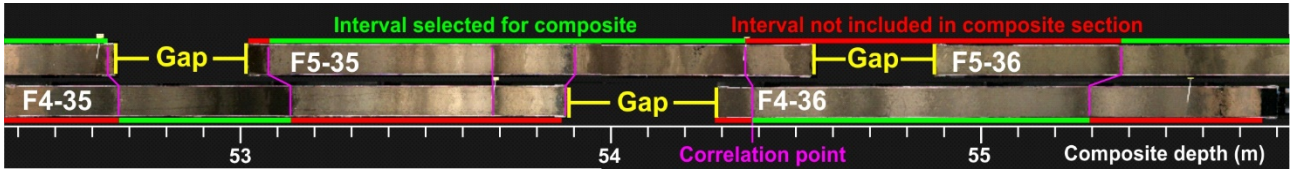


Figure 2. Example of correlation between the overlapped F4 and F5 core sections and of the selection of the intervals used for building the composite F4-F5 record. Note that the gaps in-between two consecutive individual core sections of F4 borehole are documented in F5 borehole, and vice versa.

F5 investigated in this study. **(d)** Inclination data after the 16 mT AF step with tentative position of the Laschamp (LE) Blake and Iceland Basin (IBE) geomagnetic excursions. **(e)** Complete tephra record and Ca counts from XRF scanning in core F4-F5. Five stratigraphic intervals with relatively high Ca counts are highlighted in yellow and correlated to the warm Marine Isotope Stage (MIS) 1 to 11 (the threshold is at 22700 cps, see text for explanation). **(f)** Complete tephra record and Ca counts from XRF scanning in core F1-F3 (Giaccio et al., 2017; Mannella et al., 2019). **(g)** Combined tephrochronology of F1-F3 and F4-F5 core. **(h)** LR04 stack of marine benthic oxygen isotope records (Lisiecki and Raymo, 2005). Data source: $^{40}\text{Ar}/^{39}\text{Ar}$, ^{14}C , astrochronological, modelled ages and correlation of tephra of the last 190 kyr: Giaccio et al. (2017) and Mannella et al. (2019) and reference therein. The boundaries of the marine isotope stages (MIS) are according to Railsback et al. (2015).

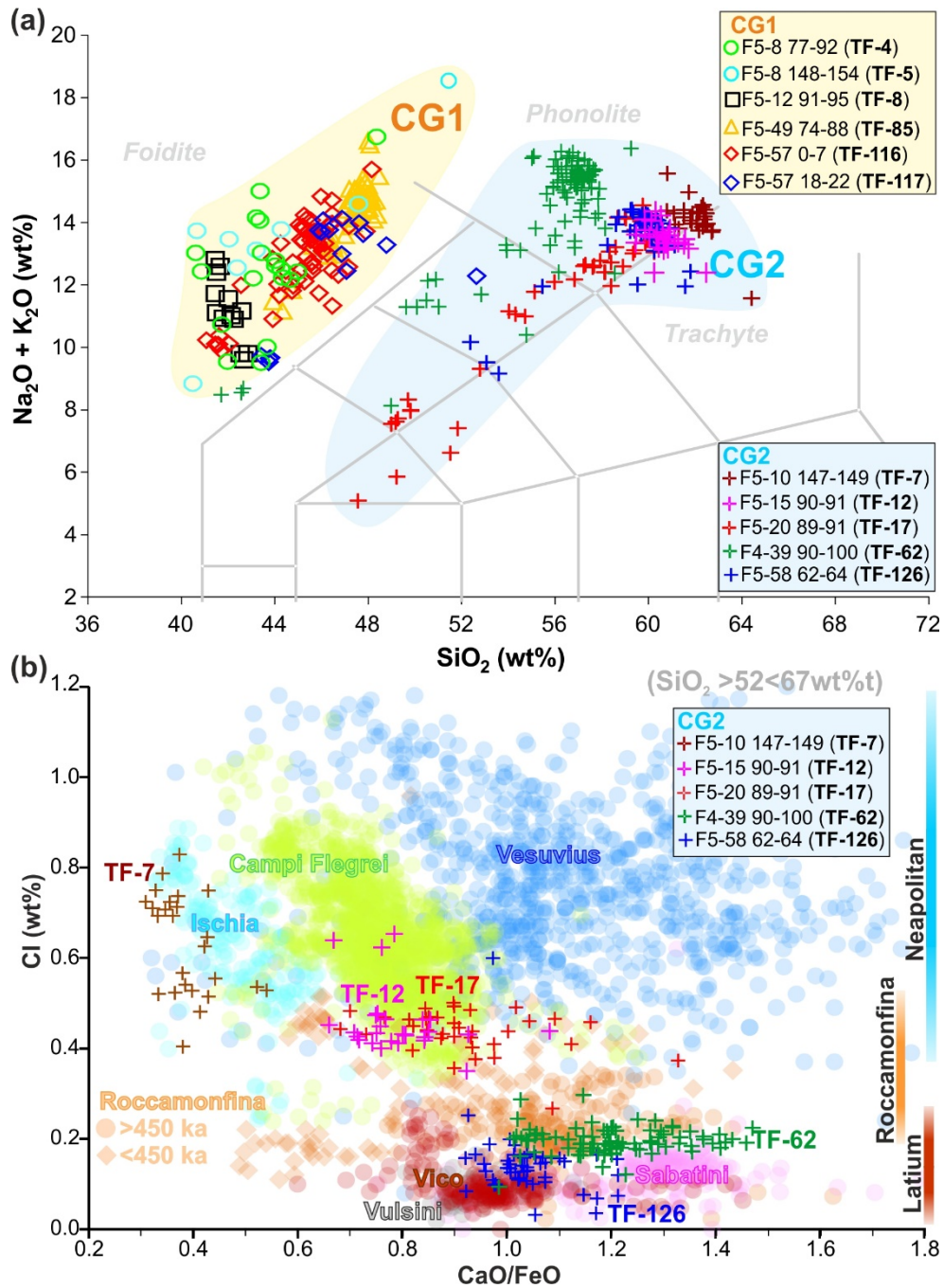


Figure 4. Representative major element compositions for the analysed F4-F5 tephra layers. **(a)** Total alkali versus silica classification diagram (Le Bas et al., 1986) of the F4-F5 tephra distinguished in two compositional groups (CG1 and CG2). **(b)** CaO/FeO vs Cl discriminating diagram of the volcanic sources of the Italian

potassic trachyte-phonolite and tephriphonolite tephra (modified from Giaccio et al., 2017) for the F4-F5 tephra. The CaO/FeO vs Cl diagram has been updated with the following data: Roccamonfina: Amato et al. (2014) and Galli et al. (2017); Vulcini, Vico Period I (P-I) and Period II (P-II) and Sabatini: this study and Author's unpublished data. For other references, the readers are referred to Giaccio et al. (2017).

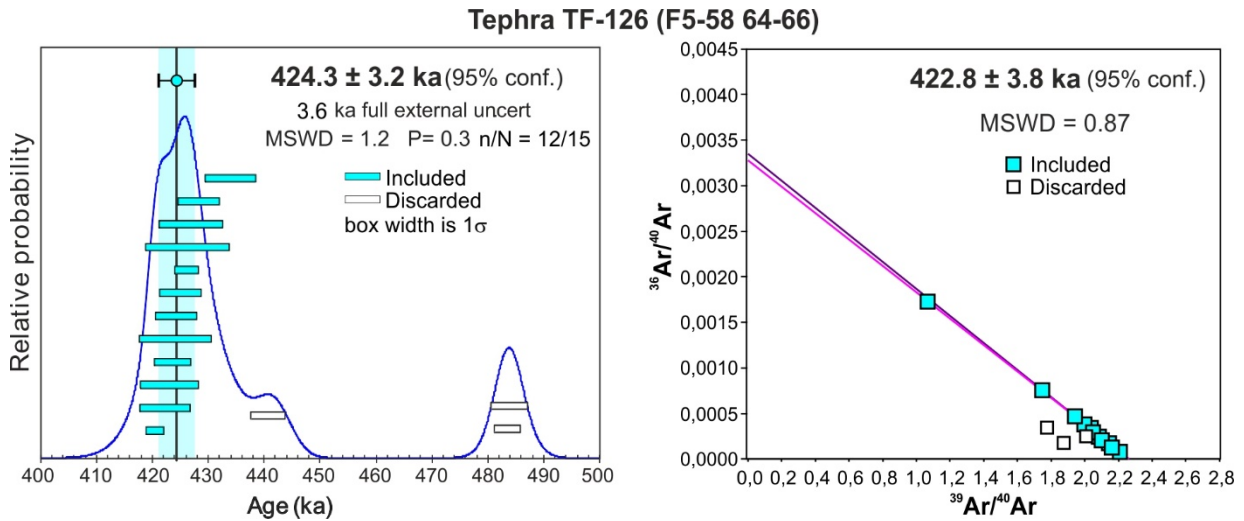
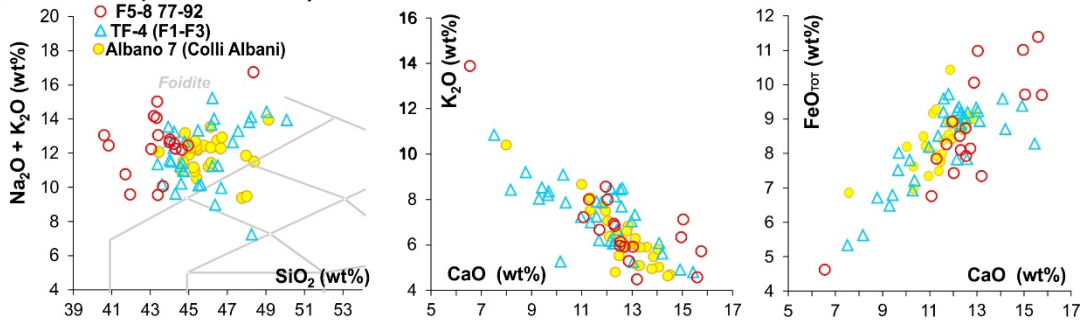
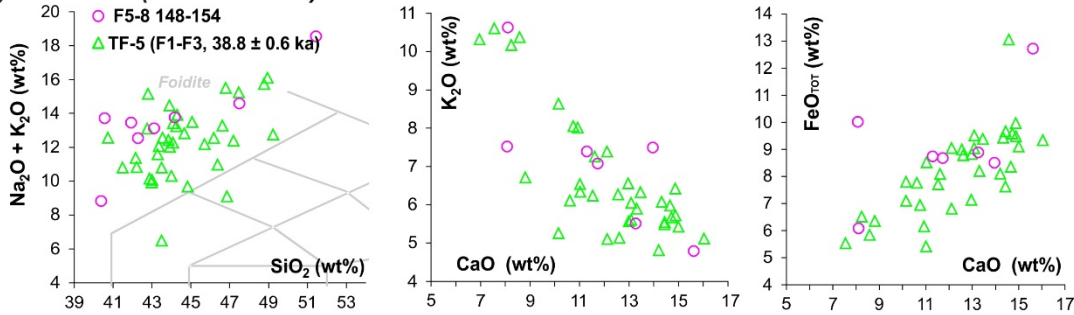


Figure 5. Age probability density spectra diagram (left) and inverse isochrone (right) of tephra TF-126 (sampling code; F5-58 64-66). Blue and white bars/ indicate the individual ages included and discarded as weighted mean age, respectively.

(a) Albano 7 (35.8 ± 1.2 ka)



(b) Albano 5 (38.8 ± 1.4 ka)



(c) Albano 3 (70.0 ± 2.0 ka)

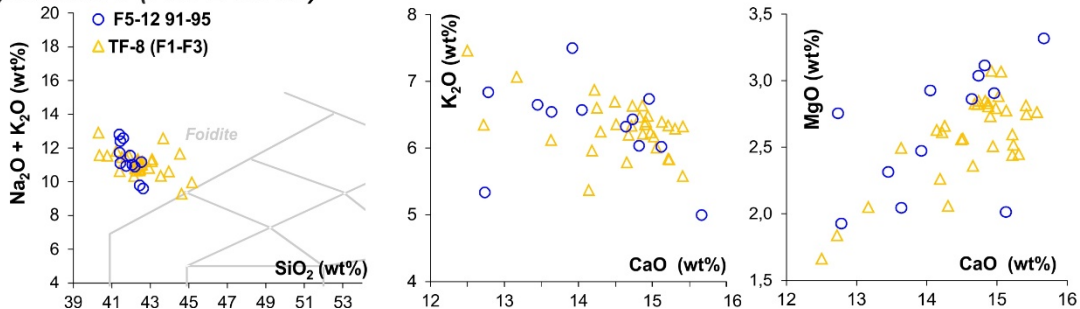
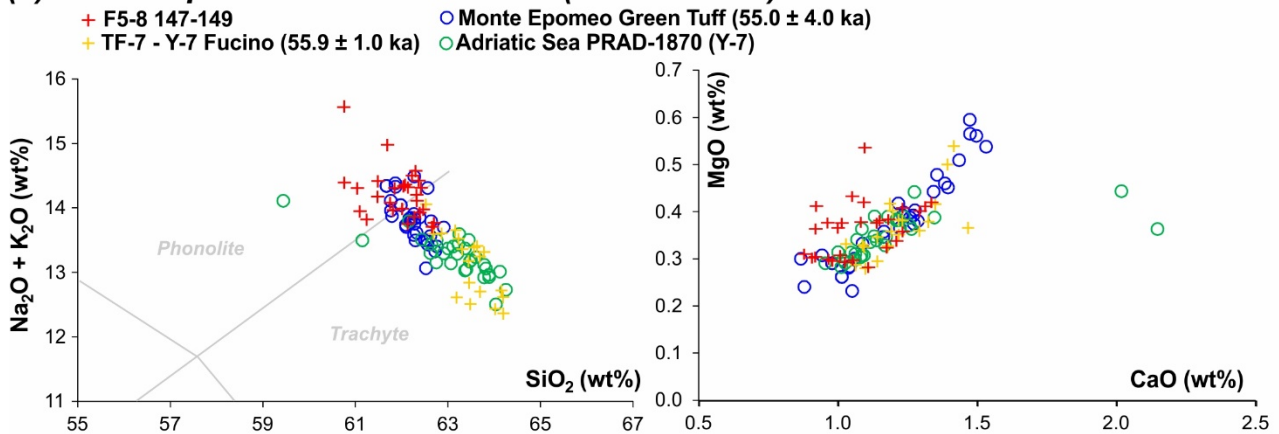
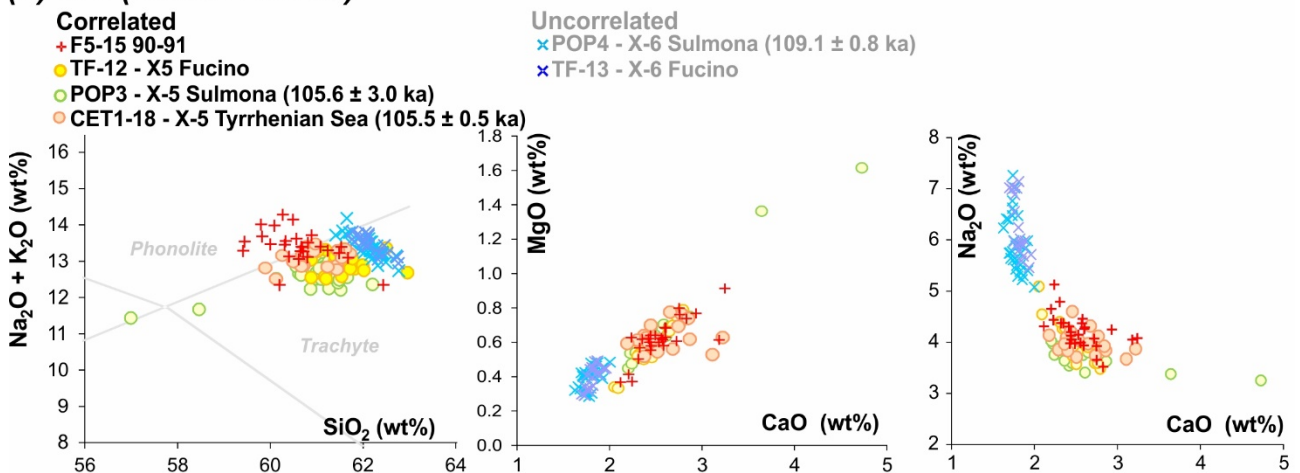


Figure 6. Total alkali versus silica classification diagram after Le Bas et al. (1986) and representative bi-plots for the tephra F5-8 77-92 (a), F5-8 148-155 (b) and F8-12 89-91 (c) from the F4-F5 record compared with their equivalents in core F1-F3. Data source: glass-WDS of Fucino TF-4, TF-5 and TF-8: Giaccio et al. (2017); $^{40}\text{Ar}/^{39}\text{Ar}$ age of Fucino TF-5: weighted mean of dating from (Freda et al., 2006; Giaccio et al., 2009; Giaccio et al., 2017), and Mannella et al. (2019); glass composition of Albano 7 Colli Albani: Giaccio et al. (2007); $^{40}\text{Ar}/^{39}\text{Ar}$ age of Albano 7 and Albano 3: weighted mean of dating from Freda et al. (2006) and Giaccio et al. (2007). $^{40}\text{Ar}/^{39}\text{Ar}$ ages are recalculated relative to an age of 1.1891 Ma for the Alder Creek sanidine monitor standard (Niespolo et al., 2017), with the uncertainty expressed at 2σ .

(a) Monte Epomeo Green Tuff - Y-7 (55.9 ± 1.0 ka)



(b) X-5 (105.6 ± 0.5 ka)



(c) Taurano Ignimbrite (159.4 ± 1.6 ka)

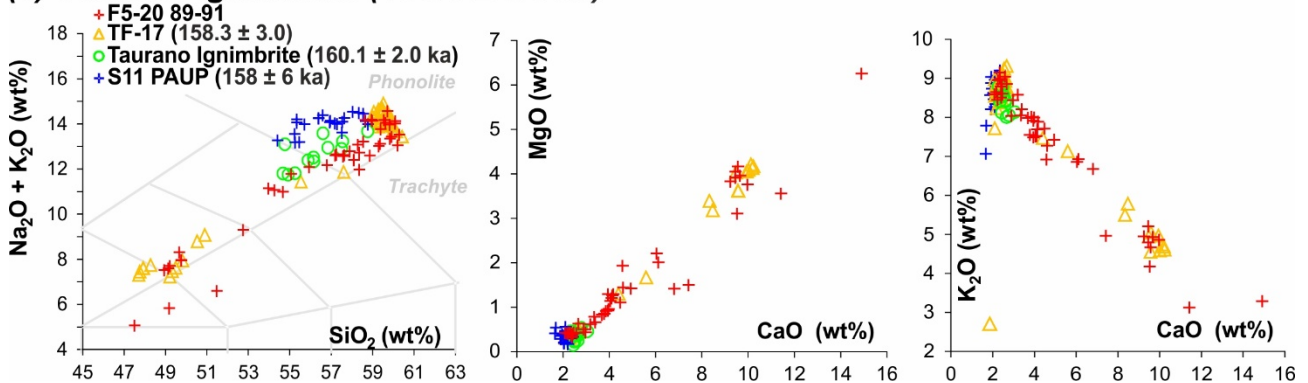
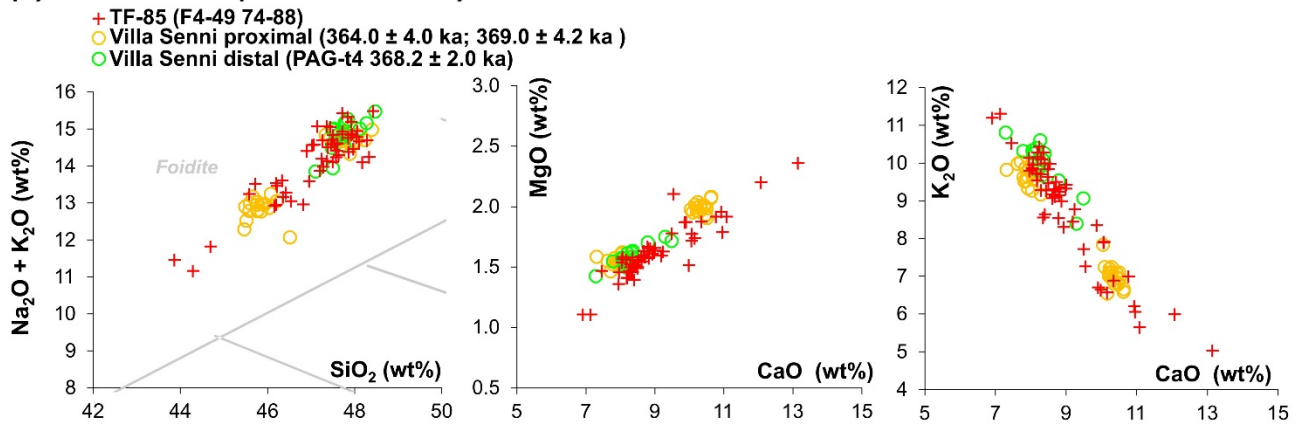


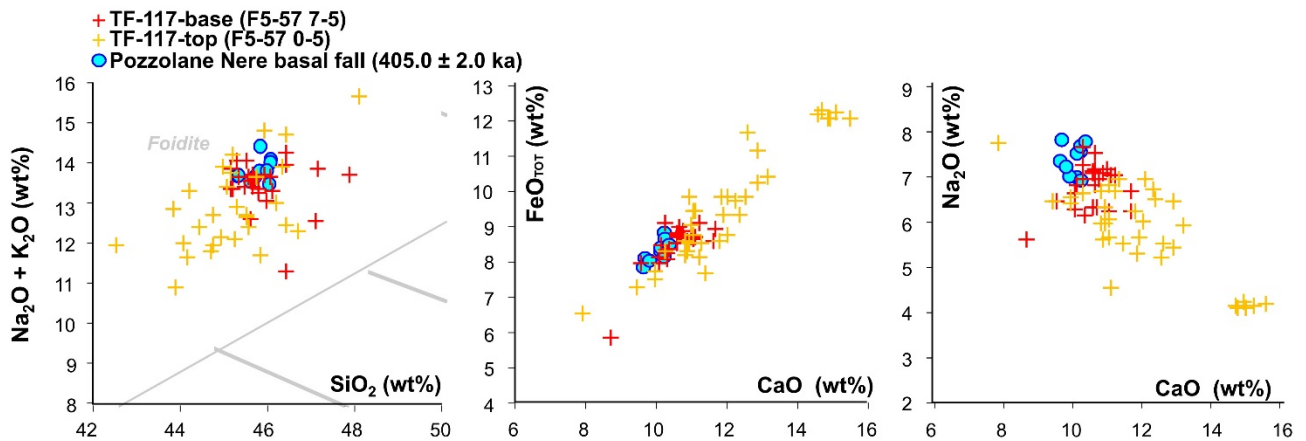
Figure 7. Total alkali versus silica classification diagram Le Bas et al. (1986) and representative bi-plots for the tephra F5-8 148-149 (a), F5-15 90-91 (b), F5-20 89-91 (c) from core F4-F5 compared with their equivalents in core F1-F3 and with some selected proximal or distal counterparts. For comparison, in panel (b) also the composition of X-6 layer (grey text), not correlated with F5-15 90-91, is shown. Data source: glass-WDS and

$^{40}\text{Ar}/^{39}\text{Ar}$ age of Fucino TF-7: Giaccio et al. (2017); glass-WDS and $^{40}\text{Ar}/^{39}\text{Ar}$ age of Monte Epomeo Green Tuff: Tomlinson et al. (2014)) and Sbrana and Toccaceli (2011), respectively; glass-WDS of PRAD-1870: Bourne et al. (2010); glass-WDS TF-12 and TF-13 Giaccio et al. (2017); glass-WDS and $^{40}\text{Ar}/^{39}\text{Ar}$ age of Sulmona POP3 and POP4 tephra layers: Giaccio et al. (2012b) and Regattieri et al. (2015), respectively; glass-EDS glass-WDS and $^{40}\text{Ar}/^{39}\text{Ar}$ age of TF-17: Giaccio et al. (2017); glass-EDS and $^{40}\text{Ar}/^{39}\text{Ar}$ age of CET1-18: Petrosino et al. (2016); glass-EDS and $^{40}\text{Ar}/^{39}\text{Ar}$ age of the proximal Taurano Ignimbrite: Amato et al. (2018) and De Vivo et al. (2001), respectively; glass-EDS and $^{40}\text{Ar}/^{39}\text{Ar}$ age of S11 PAUP: Amato et al. (2018). The tephra age reported on top of each figure panel is the weighted mean of the $^{40}\text{Ar}/^{39}\text{Ar}$ ages indicated in the respective panel. $^{40}\text{Ar}/^{39}\text{Ar}$ ages are recalculated relatively to an age of 1.1891 Ma for the Alder Creek sanidine monitor standard (Niespolo et al., 2017), with the uncertainty expressed at 2σ .

(a) Villa Senni (367.5 ± 1.6 ka)



(b) Pozzolane Nere (405.0 ± 2.0 ka)



(c) Pozzolane Nere precursor (407.1 ± 4.2 ka)

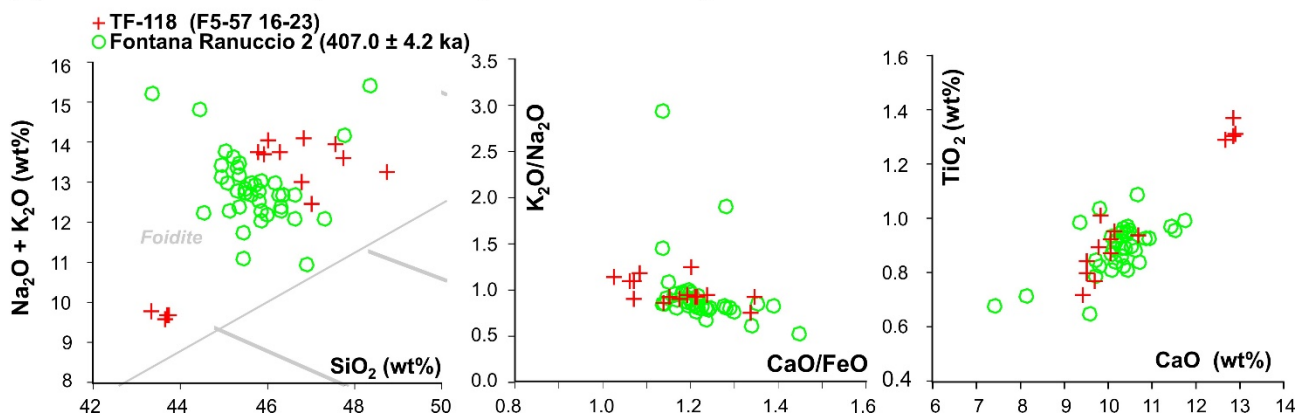
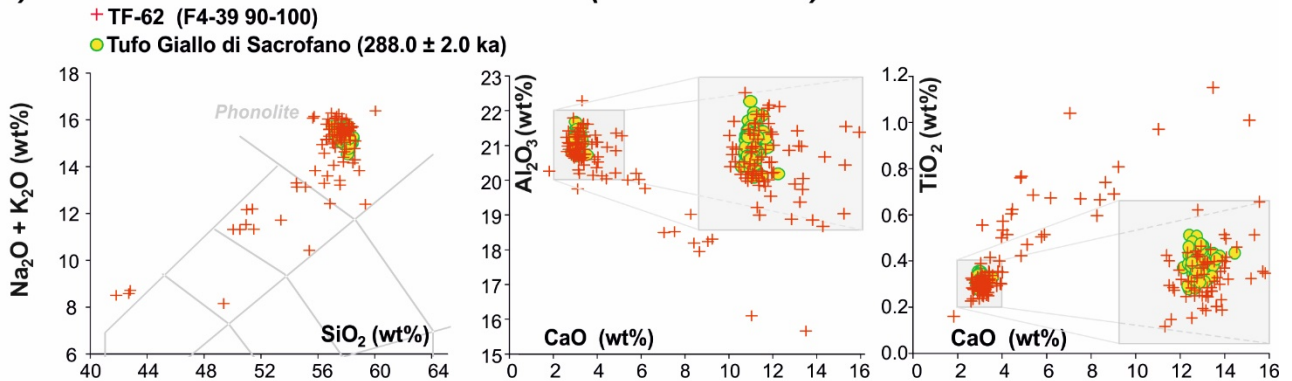


Figure 8. Total alkali versus silica classification diagram after Le Bas et al. (1986) and representative bi-plots for the tephra TF-85 (a), TF-117 (b), and TF-118 (c) from the F4-F5 record compared with their proximal or distal counterparts. Data source: glass-WDS and $^{40}\text{Ar}/^{39}\text{Ar}$ age of Villa Senni proximal units: (Marra et al., 2009, 2019); glass-WDS and $^{40}\text{Ar}/^{39}\text{Ar}$ age of Villa Senni distal (PAG-t4): (Giaccio et al., 2012a); glass-WDS and $^{40}\text{Ar}/^{39}\text{Ar}$ age Pozzolane Nere fallout: (glass-WDS): (Marra et al., 2009); glass-WDS and $^{40}\text{Ar}/^{39}\text{Ar}$ age Fontana Ranuccio 2 (glass-WDS): (Pereira et al., 2018). The tephra age reported on top of each figure panel is the weighted mean of the $^{40}\text{Ar}/^{39}\text{Ar}$ ages indicated in the respective panel. $^{40}\text{Ar}/^{39}\text{Ar}$ ages are recalculated

(a) Sabatini - Tufo Giallo di Sacrofano (288.0 ± 2.0 ka)



(b) Vulsini - Castel Broco (424.3 ± 3.2 ka)

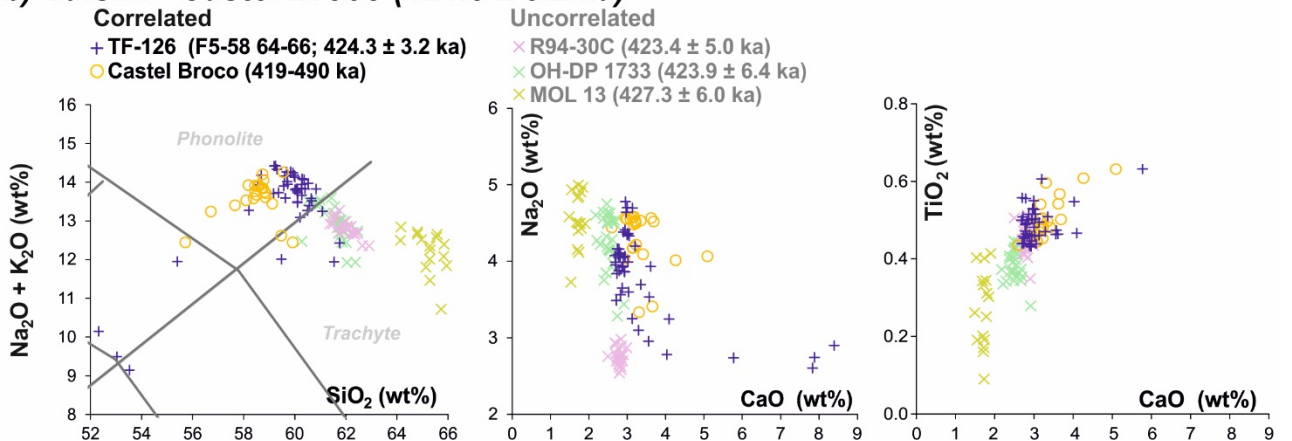


Figure 9. Total alkali versus silica classification diagram after Le Bas et al. (1986) and representative bi-plots for the tephra TF-62 (a) and TF-126 (b) of the F4-F5 succession compared with their proximal counterparts. TF-126 is also compared with some geochronologically compatible but geochemically different tephra R99-30C (Tiber River successions), OH-DP 1733 (Lake Ohrid) and MOL 13 (Bojano Basin). Data source: glass-WDS of Tufo Giallo di Sacrofano and Castel Broco: this study; $^{40}\text{Ar}/^{39}\text{Ar}$ age of Tufo Giallo di Sacrofano: Sottili et al. (2010); glass-WDS and $^{40}\text{Ar}/^{39}\text{Ar}$ age of R94-30C: this study and Marra et al. (2016) respectively; glass-WDS of OH-DP 1733: Leicher et al. (in review); glass-WDS of MOL 13: Amato et al. (2014). The tephra age reported on top of each figure panel is the weighted mean of the $^{40}\text{Ar}/^{39}\text{Ar}$ ages indicated in the respective panel. $^{40}\text{Ar}/^{39}\text{Ar}$ ages are recalculated relatively to an age of 1.1891 Ma for the Alder Creek sanidine monitor standard (Niespolo et al., 2017), with the uncertainty expressed at 2σ .

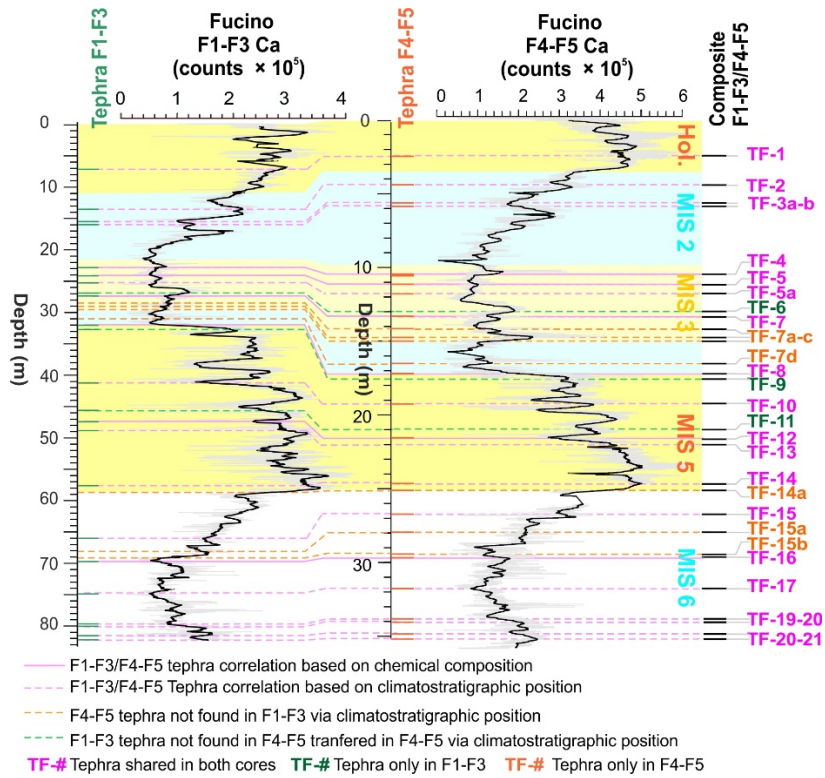


Figure 10. Detailed proxy and tephra correlation of the F1-F3 record with the corresponding interval in core F4-F5. The two tephra records are merged for a composite F1-F3/F4-F5 tephra record. Note that tephra found only in F1-F3 or F4-F5 are transferred from one to the other via climatostratigraphic positions.

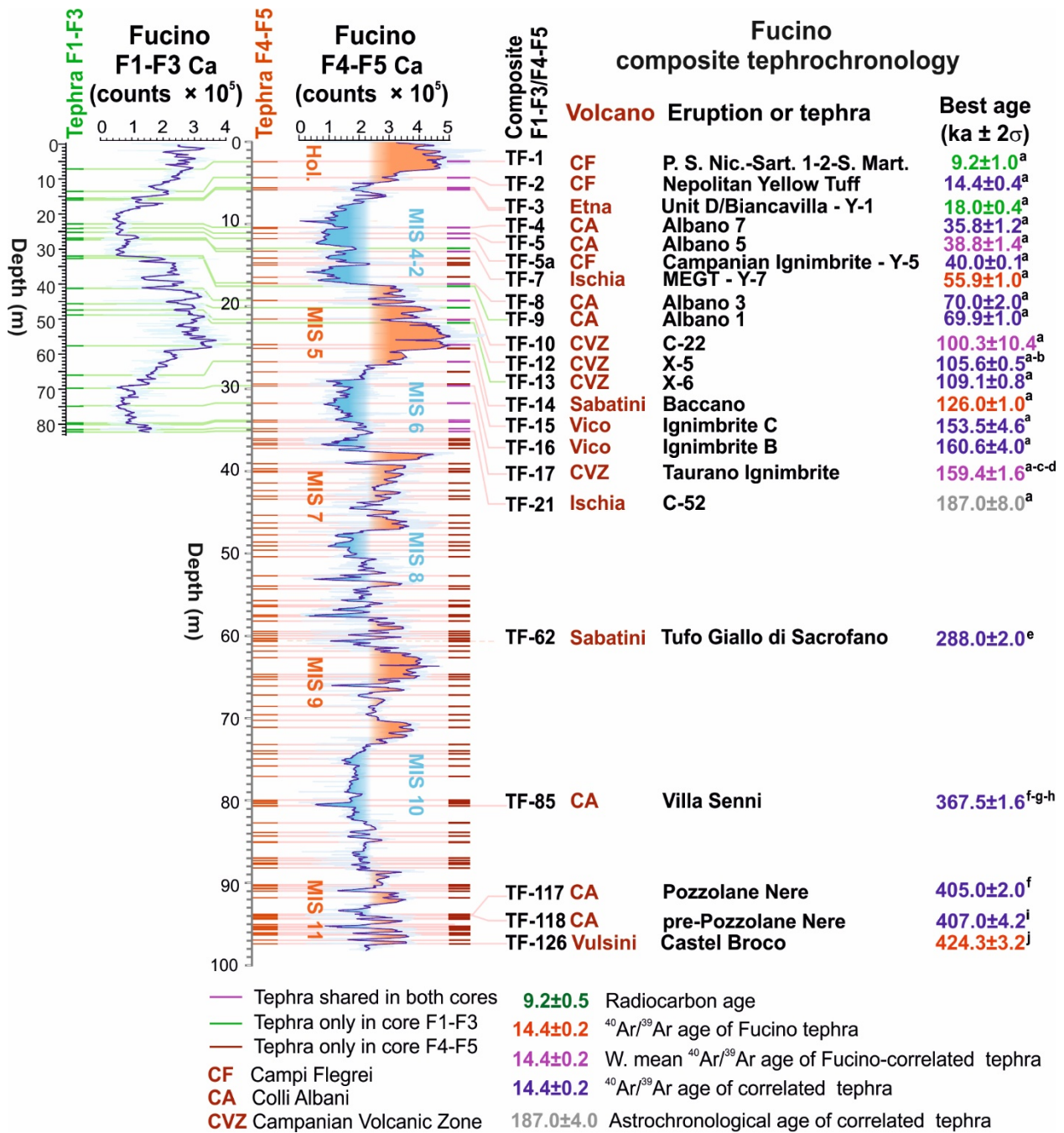


Figure 11. Composite F1-F3/F4-F5 tephra record. References: ^a Mannella et al. (2019 and references therein); ^b Petrosino et al. (2016) ^c Amato et al. (2018); ^d De Vivo et al.. (2001); ^e Sottili et al. (2010); ^f Marra et al. (2009); ^g Marra et al. (2019); ^h Giaccio et al. (2012); ⁱ Pereira et al. (2018); ^j This study. ⁴⁰Ar/³⁹Ar ages are recalculated relatively to an age of 1.1891 Ma for the Alder Creek sanidine monitor standard (Niespolo et al., 2017), with the uncertainty expressed at 2σ.

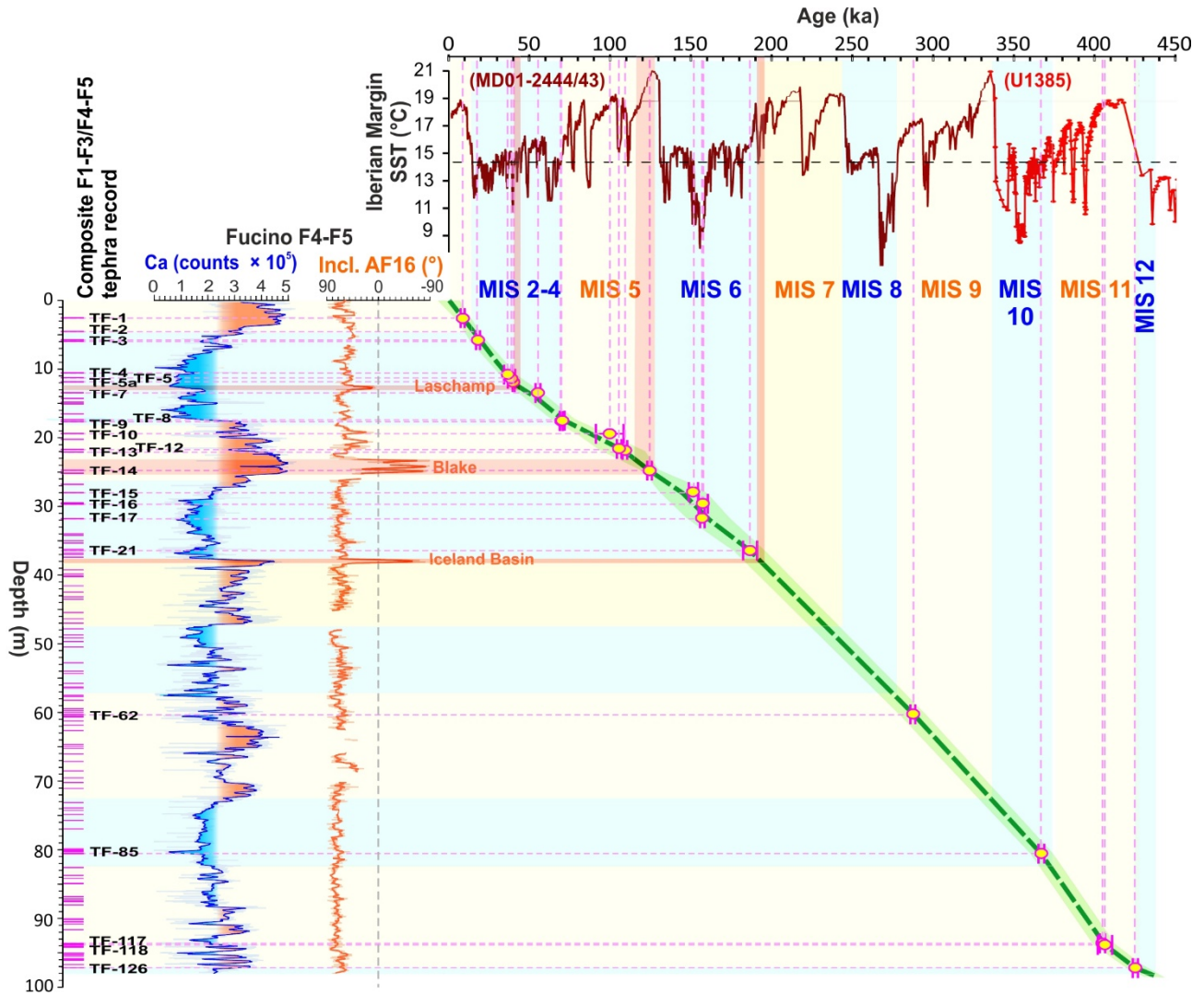


Figure 12. Preliminary age model for the composite F1-F3/F4-F5 tephra and F4-F5 Ca and palaeomagnetic records. The Fucino calcium record is compared with the sea surface temperature (SST) record from the SW Iberian Margin core MD01-2444/43 (dark red, Martrat et al., 2007) and core U1385 (red Rodrigues et al., 2017). The boundaries of the marine isotope stages (MIS) Iberian Margin record and are projected in the Fucino record along the intercept points of the yellow/blue bars with the dashed green line, which is the linear interpolation between the mid-point of the tephra ages reported in Figure 9. The ages of Fucino tephras (dashed pink lines) are in turn projected in the time-scale of the Iberian Margin SST records, that are based on their own age models (Martrat et al., 2007; Rodrigues et al., 2011). The interceptions of the orange bars with the dashed green line also provide an age estimation for the Laschamp, Blake and Iceland Basin geomagnetic excursions, as inferred from the preliminary palaeomagnetic data.

Table 1: Analysed tephra layers from core F4-F5.

Fucino tephra	Sampling code	Bottom mcd	Thickness (cm)	Main lithological features	Source
TF-4	F5-8 77-93	10.57	15.50	Darkish coarse ash made of dense blackish porphyritic scoria including crystals of leucite, pyroxene and dark mica, also occurring as abundant loose clasts. Accessory lithic made of lava and holocrystalline clasts also occur.	Colli Albani
TF-5	F5-8 148-154	11.13	~6*	Darkish coarse ash made of dense blackish porphyritic scoria including crystals of leucite, pyroxene and dark mica, also occurring as abundant loose clasts. Accessory lithic made of lava and holocrystalline clast also occur.	Colli Albani
TF-7	F5-10 147-149	14.14	2.00	Greyish medium ash made of whitish-transparent micro-pumices associated with dense brownish glass shards with abundant loose crystals of large sanidine and black mica.	Ischia
TF-8	F5-12 90-95	17.15	4.50	Darkish ash made of blackish poorly vesicular scoria associated to scarce crystals of leucite and clinopyroxene.	Colli Albani
TF-12	F5-15 90-91	21.53	1.00	Greyish to dark yellow, fine grained ash with whitish-transparent micropumices and glass shards. Stretched/elongated vesicles, only very few loose crystals of sanidine, black mica and pyroxene.	Campi Flegrei-CVZ
TF-17	F5-20 89-91	29.64	2.00	Fine to coarse grained, greyish ash with 1) greyish dark vesicular scoria; 2) brownish and transparent glass shards and micropumice; 3) coarse, (rounded) whitish and greyish pumice, with loose sanidine, clinopyroxene, and amphibole crystals	Campi Flegrei-CVZ
TF-62	F4-39 90-100	60.60	10.00	Darkish coarse ash consisting of 1) greyish dark vesicular scoria; 2) brownish and transparent glass shards and micropumice; 3) coarse, (rounded) whitish and greyish pumice, with loose sanidine, clinopyroxene, and amphibole crystals.	Sabatini
TF-85	F5-49 74-88	80.52	13.25	Darkish medium-coarse ash made of both black porphyritic leucite-bearing scoriae and aphyric highly vesicular black scoriae, along with abundant crystals of leucite and dark mica and lithics. Toward the top, the ash becomes finer.	Colli Albani
TF-117	F5-57 0-7	95.13	7.00	Darkish fine ash made of black porphyritic leucite-bearing scoriae associated with free crystals of leucite and lithics. Toward the top, the sediment evolves into a coarse ash made of blackish vesicular porphyritic scoriae along with leucite and lithics.	Colli Albani
TF-118	F5-57 16-23	95.29	7.50	Darkish fine ash made of black porphyritic scoriae along with abundant free crystals of leucite and minor lithics.	Colli Albani
TF-126	F5-58 64- 66	97.24	2.00	Light-grey medium ash made of highly vesicular white pumices associated with crystals of sanidine, plagioclase, dark mica and opaques and glass shards and minor lithics. Toward the top, the sediment turns to a dark grey-blackish medium ash.	Vulsini

*Base of tephra inside of the core-catcher, not in composite depth.

Supplementary materials

SD1: Full data set of the tephra glass major element composition (WDS-EMPA).

SD2: Full data set of the $^{40}\text{Ar}/^{39}\text{Ar}$ dating.

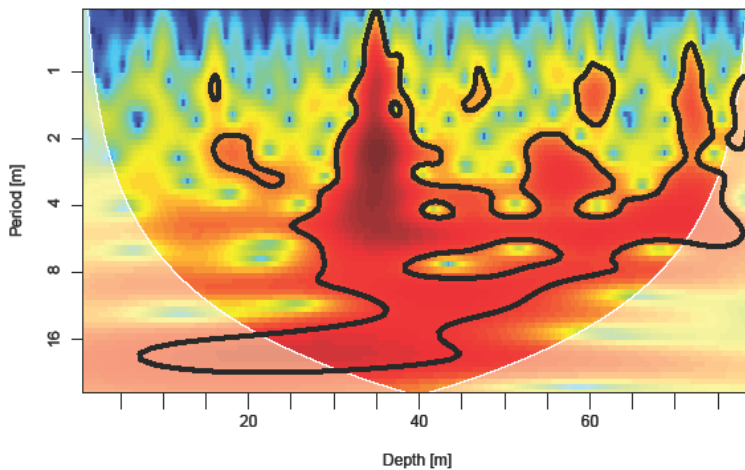


Figure S1. Wavelet analysis of the gamma ray dataset from F4 borehole. The white shading indicates areas outside the cone of influence that should be taken with care. Red colours indicate strong cyclicity, and blue colours no cyclic behaviour of the data. The bold line represents the results of a significance test, for details see Gouhier et al. (2018) and the appended R script.